

PH.D THESIS

**ȘTEFAN CEL MARE UNIVERSITY OF SUCEAVA AND PARIS-SACLAY
UNIVERSITY
PREPARED AT FACULTY OF ELECTRICAL ENGINEERING AND COMPUTER
SCIENCE AND AT SAINT QUENTIN EN YVELINES UNIVERSITY OF
VERSAILLES**

DOMAIN: COMPUTERS AND INFORMATION TECHNOLOGY

BY

CĂTĂLIN MARICEL JURESCHI

SUBJECT:

TEMPERATURE AND PRESSURE SENSORS BASED ON MOLECULAR SPIN
TRANSITION MATERIALS

Supervisors:

Prof. Yasser ALAYLI

Prof. Jorge LINARES

Prof. Corneliu Octavian TURCU

Contents

Introduction	1
1 State of the art	6
1.1 Introduction	6
1.2 The spin transition induced by temperature	8
1.3 The spin transition induced by pressure	8
1.4 Theory. Models and methods	9
1.4.1 Ising-like model.....	9
1.4.2 Atom phonon coupling model.....	10
1.4.3 Monte Carlo Metropolis	10
1.4.4 Monte Carlo entropic sampling.....	11
2 Sensing applications of SCO materials.....	13
2.1 Introduction	13
2.2 Temperature sensors	13
2.3 Pressure sensors	15
3 Cooperativity tuning in spin crossover nanostructures via matrix and architecture effect.....	17
3.1 Introduction	17
3.2 Matrix effect on spin crossover nanoparticles on the origin of multi-step spin transition behavior in 1D nanoparticles.....	17
3.2.1 The Ising-like model with edge effect.....	17
3.3 Size dependence of the equilibrium temperature in 2D SCO system.....	21
3.4 Analysis of edge effect in 3D systems.....	23
3.4.1 Results and discussions	23
3.5 Analysis of architecture effect.....	24
4 Analysis of spin crossover nanochains using parabolic approximation in the framework of Atom-phonon coupling model	27
4.1 Introduction	27
4.2 The model.....	28
4.3 Results and discussions	28
4.3.1 Role of parameters in the parabolic algorithm.....	29
4.3.2 Entropy variation and heat capacity using the dynamic matrix method vs. the parabolic method.....	31

4.4	The role of edge atoms using the dynamic matrix transfer and the free energy methods.....	32
5	Pressure effect in molecular spin crossover compounds	35
5.1	Analysis of the P-T- n_{HS} phase diagram of $[Fe(hyprtz)]A_2 \cdot H_2O$ spin crossover 1D coordination polymer.....	35
5.1.1	Pressure effect	35
5.1.2	Pressure-Temperature (p-T) phase diagram.....	36
5.2	Impact detection using SCO materials	38
5.2.1	Results and discussions	38
5.3	Sensor concept.....	41
	General Conclusions	43
	References	45

List of figures

Figure 1 Analysis and Forecast of the World market of sensors until 2016: subdivision by regions [6]	2
Figure 2 The evolution of sensors market [9].....	3
Figure 1.1 Representation of the five 3d orbitals.	7
Figure 1.2 Electronic diagram of the HS and LS state for a Fe(II) ion in an octahedral ligand field.....	7
Figure 1.3 Various types of thermal induced spin transition: a) with hysteresis, b) gradual, c) two steps transition, d) incomplete [84,85]	8
Figure 1.4 Schematic representation of the pressure influence.	8
Figure 2.1 The color changes and electron distribution of Fe(II) in the LS and HS states. [100].....	13
Figure 2.2 Change of color in the SCO liquid crystalline films around 60 °C of $[\text{Fe}(\text{C}_n\text{-trz})_3](4\text{-MeC}_6\text{H}_4\text{SO}_3)_2 \cdot \text{H}_2\text{O}$ [101].....	13
Figure 2.3 The thermal variation of magnetic proprieties of the complexes (a) $[\text{Fe}(\text{C}_n\text{-trz})_3](4\text{-MeC}_6\text{H}_4\text{SO}_3)_2 \cdot \text{H}_2\text{O}$ (for the cases 1 - $n=8$, 2 - $n=10$ and 3 - $n=12$) and (b) $[\text{Fe}(\text{C}_n\text{-trz})_3](4\text{-MeC}_6\text{H}_4\text{SO}_3)_2 - n=12$ [101].	14
Figure 2.4 (a) Magnetic thermal hysteresis for compound $[\text{Fe}(\text{Htrz})_2(\text{trz})](\text{BF}_4)$; (b) The colors at room temperature in the low spin state (left) and the high spin state (right).....	14
Figure 2.5 Example of sensor using SCO compounds [103]	15
Figure 2.6 Schematic representation of the pressure influence on the LS and HS potential wells of an Fe(II) SCO compound [104].	15
Figure 2.7 The operating principle of a SCO sensor with optical reflectivity detection [25].	16
Figure 2.8 Types of pigments and their applications [106].	16
Figure 3.1 Thermal evolution of the HS molar fraction, n_{HS} , in a 1D SCO system embedded into a matrix for different matrix interaction strength: Square ($L/k_B = 90$ K), Circle ($L/k_B = 147$ K) and Triangle ($L/k_B = 180$ K). The parameter values are: $N = 16$ molecules, $\Delta/k_B = 240$ K, $\ln(g) = 9.5$, $G/k_B = 120$ K, and $J/k_B = -43$ K.	19
Figure 3.2 Evolution of the HS molar fraction, n_{HS} , as a function of temperature, for various numbers of molecules: (a) $N=6$ molecules, (b) $N=10$ molecules, (c) $N=20$ molecules, (d) $N=38$ molecules for different polymeric-interactions strength: Square ($L/k_B = 90$ K), Circle ($L/k_B = 147$ K) and Triangle ($L/k_B = 180$ K). The computational parameters are: $\Delta/k_B = 240$ K, $\ln(g) = 9.5$, $G/k_B = 120$ K, and $J/k_B = -43$ K.	19
Figure 3.3 Evolution of the HS molar fraction n_{HS} as a function of temperature, for the case: (Circle) ($L/k_B = 147$ K, $J/k_B = -43$ K) and (Triangle) ($L/k_B = 0$ K, $J/k_B = 0$ K). The computational parameters are: $N=16$, $\Delta/k_B = 240$ K, $\ln(g) = 9.5$ and $G/k_B = 120$ K.....	20
Figure 3.4 Evolution of molecules in the HS state, n_{HS} , as a function of temperature, for a 1D system $N= 16$ molecules, for different long range-interactions strength: $G/k_B = 40$ K (triangle), $G/k_B = 80$ K (circles), $G/k_B = 120$ K (star) The parameter values are $\Delta/k_B = 240$ K, $\ln(g) = 9.5$, $J/k_B = -43$ K, and $L/k_B = 147$ K.	20
Figure 3.5 Evolution of molecules in the HS state, n_{HS} , as a function of temperature, for a 1D system $N= 16$ molecules, for different long short-interactions strength: $J/k_B = -43$ K (triangle), $J/k_B = -30$ K (circle) and $J/k_B = -20$ K (star). The parameter values are $\Delta/k_B = 240$ K, $\ln(g) = 9.5$, $G/k_B = 120$ K, and $L/k_B = 147$ K.	21
Figure 3.6 The simulated thermal behavior of the total HS fraction, $n_{\text{HS}}(T)$, for different system's sizes, showing an increase of the thermal hysteresis width for smaller nanoparticle sizes. The computational parameters are: $\Delta/k_B = 1300$ K, $G/k_B = 172.7$ K, $J/k_B = 15$ K, $L/k_B = 120$ K, $\ln(g) = 6.01$	21

Figure 3.7 The thermal behavior for the edge, inner and total molecules of the system for the cases: left - $N_t = 16$ (4x4) and right - $N_t = 144$ (12x12). The model parameters are the same as those of Figure 3.6.....	22
Figure 3.8 Simulated HS fraction, n_{HS} , as a function of temperature for a 3D SCO system. The computational parameters are $N = 125$ (5x5x5), $\Delta/k_B = 1450$ K, $G/k_B = 470$ K, $J/k_B = -100$ K, $L/k_B = 750$ K and $\ln(g) = 4.7$	23
Figure 3.9 Simulated HS fraction, n_{HS} , as a function of temperature for a 3D SCO system when $L/k_B = 0$ K. The other parameters are the same as those of figure 3.8.....	24
Figure 3.10 Simulated HS fraction, n_{HS} , as a function of temperature for 3D SCO systems of different sizes. Other parameters are the same as those of figure 3.8.	24
Figure 3.11 Evolution of HS fraction for different architectures of systems for the cases (a) $J/k_B=64$ K and (b) $J/k_B=105$ K. The computational parameters are: $\Delta / k_B = 1300$ K , $\ln(g) = 6$, $G / k_B = 105$ K [120].	25
Figure 3.12 Simulated thermal transition for different sizes of a cubic system. The inset shows the size dependence of the thermal hysteresis loop width. The parameters' values used in the simulations are $J/k_B = 45$ K, $G/k_B = 105$ K, $\Delta/k_B = 1300$ K, $\ln(g) = 6$	25
Figure 3.13 The thermal behaviour for different shapes of a 2D system containing 36 molecules. The computational parameters are: $\Delta/k_B = 1300$ K, $J/k_B = 15$ K, $G/k_B = 172.7$ K, $L/k_B = 120$ K, $\ln(g) = 6.01$, $N = 36$	26
Figure 4.1 Schematic representation of the elastic constants related to	27
Figure 4.2 Schematic representation of the possible atoms' configurations in the chain.....	28
Figure 4.3. The thermal variation of high spin fraction n_{HS} for a 1D SCO compound a) $N=8$ molecules b) $N=20$ molecules using the MFA method (circles), the Parabolic method (triangles), the Dynamic matrix (stars). Other parameter are $x=0.2$, $y=0.2$, $g=5$ and $\delta=4$	29
Figure 4.4. The thermal variation of the high spin fraction n_{HS} for a 1D SCO compound ($N=8$ molecules) for different degeneracies a) $g=5$ b) $g=150$ c) $g=1000$ d) $g=5000$ using, the Parabolic method (triangles), the Dynamic matrix (stars). Other parameter are $x=0.3$, $y=0$, and $\delta=0.6$	30
Figure 4.5. The thermal variation of n_{HS} for a 1D SCO compound ($N=8$ molecules) for different degeneracy values a) $g=5$ b) $g=150$ c) $g=1000$ d) $g=5000$ using the Parabolic method (triangle curve), the Dynamic matrix (stars curve). The following computational parameters have been used: $x=0.1$, $y=0.9$, and $\delta=0.6$	31
Figure 4.6. Time dependence of the entropy per atom obtained using: the dynamic matrix method (red curve) and the parabolic method (blue curve) for two different sizes and interactions. Other parameter are $g=1000$ and $\delta=0.6$	31
Figure 4.7. Time dependence of the heat capacity obtained using: the dynamic matrix method (red curve) and the parabolic method (blue curve) for two different sizes and interactions. Other parameter are $g=1000$ and $\delta=0.6$	32
Figure 4.8. a) the simulated HS fraction, n_{HS} , as a function of the temperature and b) the free energy for three different temperatures for an A type system.....	33
Figure 4.9 a) the simulated HS fraction, n_{HS} , as a function of the temperature and b) the free energy for three different temperatures for a B type system.	34
Figure 5.1 Simulated thermal hysteresis loop, at ambient pressure (a) and pressure hysteresis loop, recorded at 200 K (b). The values of the parameters used in calculations are: $\Delta/k_B=800$ K, $\Gamma/k_B = 300$ K, $\ln(g) = 7$ and $\delta V=13.2 \text{ \AA}^3$	36
Figure 5.2 Selected thermal (left) and pressure (right) hysteresis loops recorded at several pressures and temperatures, respectively for $[\text{Fe}(\text{hyptrz})]_2\text{A}_2\cdot\text{H}_2\text{O}$	37
Figure 5.3 Experimental 2D p-T phase diagram recorded on $[\text{Fe}(\text{hyptrz})]_2\text{A}_2\cdot\text{H}_2\text{O}$	37
Figure 5.4 Incomplete experimental 3D (p-T- n_{HS}) phase diagram recorded on $[\text{Fe}(\text{hyptrz})]_2\text{A}_2\cdot\text{H}_2\text{O}$..	38

Figure 5.5 Thermal evolution of reflectance spectra recorded on $[\text{Fe}(\text{hyetrz})_3]_2 \cdot \text{H}_2\text{O}$ in the solid state (left) and of the optical density at $\lambda = 550 \text{ nm}$ (right).	39
Figure 5.6 DSC curves for $[\text{Fe}(\text{hyetrz})_3]_2 \cdot \text{H}_2\text{O}$ over the 265-303 K temperature range.....	39
Figure 5.7 (Left): sample holder showing the SCO compound at room temperature on its sample holder covered with a scotch tape. (Right): Enlarged view of the sample evidencing colour change to pink at room temperature for various applied pressures (25 MPa, 50 MPa, 100 MPa, 150 MPa, 200 MPa and 250 MPa).....	40
Figure 5.8 Thermal dependence at 1 bar (left) and pressure dependence at 300 K (right) of the HS molar fraction, n_{HS} , as derived from the Ising like model. The parameters values are $\Delta_0/k_{\text{B}} = 1978.6 \text{ K}$, $\delta V = 100 \text{ A}^3$, $\ln(g) = 6.906$ and $\Gamma/k_{\text{B}} = 360 \text{ K}$	40
Figure 5.9 Pressure-temperature phase diagram calculated for a SCO system switching around the room temperature region using the following parameters values: $\Delta_0/k_{\text{B}} = 1978.6 \text{ K}$, $\delta V = 100 \text{ A}^3$, $\ln(g) = 6.906$ and $\Gamma/k_{\text{B}} = 360 \text{ K}$	41
Figure 5.10 Representation of the switching mechanism induced by temperature and/or by pressure.	41
Figure 5.11 Principle of measuring simultaneously temperature and pressure using two SCO compounds with optical reflectivity detection.	42

Introduction

In the broadest definition "sensor converts input signals of a physical nature into electrical output" [1]. If up until a few years ago sensors were being used for prevention purposes, today's sensors have become core elements in automation systems a sensor can perform while in operation. We can divide them into four general categories as follows:

- Monitoring, controlling and adjusting the system to increase performance;
- Security and alarm in order to enhance system security and to anticipate possible miscues;
- Diagnostics and analysis in order to better understand the operation of the system and find ways to improve it;
- Interface and navigation in order to increase functionality.

Nowadays the most used types of sensors are: transducers, functional sensors and smart sensors. Intelligent sensors distinguish themselves from other types of sensors due to their extra conditioning process control, digital interface and operating system.

It's hard to imagine today's world without automated equipment. From mobile phones, computers or washing machines to cars and airplanes, all contain sensors that make our lives easier and safer. In fact, there are no industrial areas which operate without measuring, testing, monitoring and automation. In all branches of the industry sensors are widely used to automate the production process. With the aid of sensors, the production capacity has been greatly improved and is continuously growing. This is also due to the particular concern, seen in recent years, regarding minimizing energy consumption, miniaturization, easy handling, automation and multiple use of all electronic equipment. In this respect, electronic equipment manufacturers as well as science research groups are constantly working to meet the desideratum. Special consideration is given to the development and optimization of various types of sensors with increased sensitivity and higher technical characteristics, due to the ever growing demand on the electronics market. In this high-tech field Europe, and especially Germany, holds a leading global position, not only in terms of technological standards but also in terms of global market shares. A comparison between commercial studies [2,3] in terms of demand and the results of surveys conducted by the Association for Sensors and Measurement (AMA) [4] on the sensor suppliers market, shows that European suppliers cover about 35 % of the global demand for sensors. The AMA [5] estimates that around 1000 industrial sensors manufacturers are located in Europe as compared to 3000 worldwide.

In 2012, INTECHNO CONSULTING in a report of 1520 pages [6] concerning the sensor elements, sensor modules, sensors and sensor systems, has reported an annual growth rate of non-military world market for sensors of 7.9% between 2006 and 2011 with a worldwide market sensors of 81.6 billion euros in 2006 increasing at 119.4 billion euros in 2011 and forecasted at 184.1 billion euros by the end of 2016. In this report a slight decrease in the percentage of Europe's sensors market in 2016 is noted in Figure 1.

The market for sensor technology is highly heterogeneous and difficult to break down even for those directly involved. However, a noticeable shift from the market for capital goods to the consumer goods market is being observed, with increasing emphasis on the final products. Therefore, the consumer end products sensor market has, in general, a faster growth rate than the measurement focused products and control technologies. New applications, at

considerable growth rates, are being found in domestic equipment, safety and security tools, diagnostic and therapeutic medical equipment and automotive engineering. The highest growth rates are being recorded for image sensors, acceleration sensors, pressure sensors, position and proximity sensors as well as biochemical sensors [7] The use of these sensors on an ever larger scale has resulted in a reduced price and stimulated the increase in production of sensors. A graph of the sensor market developments in the past 10 years is shown in Figure 2. It can be seen that the market grew by 6.3% on average each year albeit with a significant decline in 2008-2009 due to global crisis.

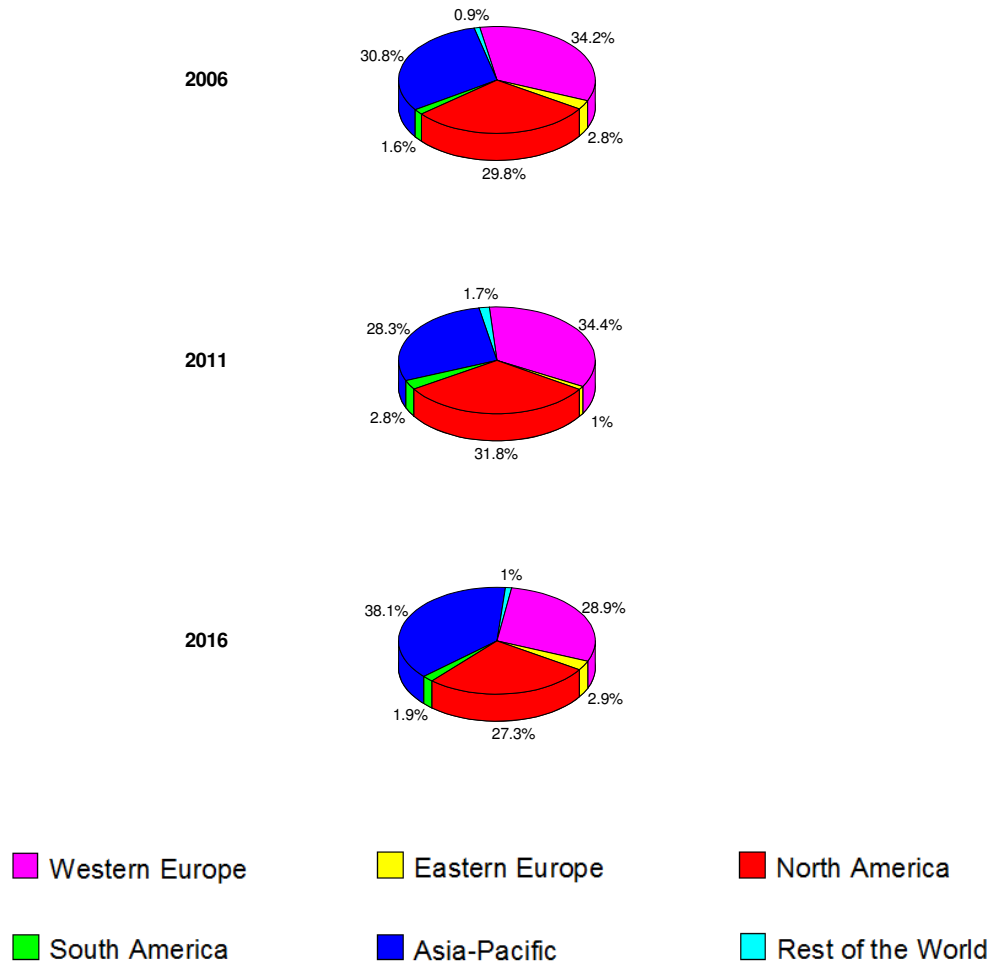


Figure 1 Analysis and Forecast of the World market of sensors until 2016: subdivision by regions [6]

SensorsPortal has published an estimation of sensors market evolution for the next 5 years [8]. The global sensors market is expected to grow from 95.3 billion dollars in 2015 to 154.4 billion dollars by 2020 with an annual growth rate of 10.1% for a period of 5 years, between 2015 and 2020. The growth rate of image, flow and level sensors is expected to increase by 11.7% over the next five years and go from 25.6 billion dollars in 2014, 28.9 billion dollars in 2015 to almost 50.2 billion in 2020. Chemical sensors and bio-sensors, an important segment of the sensor market, is expecting to grow in 2015 to 19 billion dollars. With a growth rate of 11.5%, analysts anticipate a growth to nearly 32.8 billion dollars in 2020. Intelligent sensors market is expected to grow to 10.46 billion dollars in 2020, a 36.25% growth rate from 2014 to 2020. US made sensors market, with a 30% growth rate, is expected to reach 438 million dollars by 2018. An important role in maintaining the stability

of this segment of activity is reinvestment by the industry of 10% of its turnover in research, innovation and development.

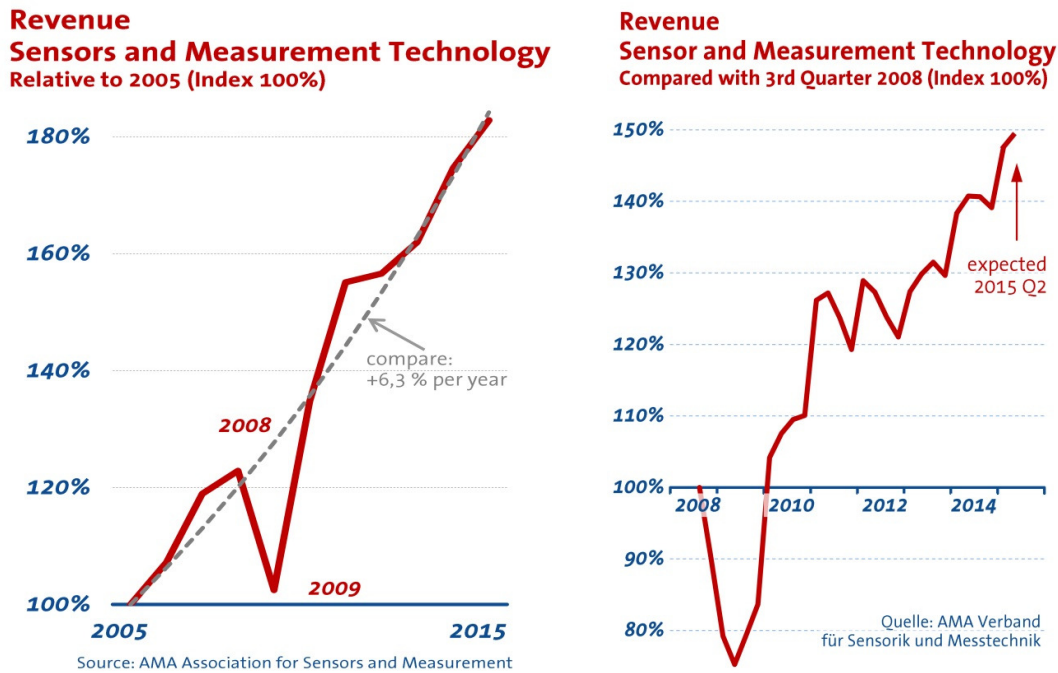


Figure 2 The evolution of sensors market [9]

Depending on the classification criteria of sensors, start from very simple to very complex sensors. Thus, depending of the errors of measurement, the sensors are classified by deviation and resolution. Other classification criteria for classification sensors are after specifications (price, size, weight, stability, linearity, resolution, switching signal, ...), material (organic, inorganic, conductor, insulator, ...) phenomenon of conversion (thermoelectric, piezoelectric, photoelectric, fotomagnetic, magneto, Termoopt, fotoelastic, electroelastic, chemical, biological, ...), scope (agriculture, construction, automotive, military, marine, ...) stimuli (acoustic biological, chemical, electrical, magnetic, optical, mechanical, thermal, piezo, ...).

An important category of sensors are temperature sensors. These sensors vary from very simple, thermostatic on / off used in domestic devices (eg. water heater) to the semiconductor sensor with a high sensitivity used in complex processes (eg. the control of furnace plant). Also, these sensors can be divided into two basic types:

- sensors which require contact with the object whose temperature it is desired to monitor and are called contact temperature sensors;
- sensors which use convection and radiation to monitor temperature change and are called non-contact sensors.

In turn, these two types of sensors can be subdivided in other basic types: thermocouples, resistive temperature sensors (RTDs - resistance temperature detectors, thermistors), infrared, bimetallic, sensors with liquid dilator, sensors that changes its molecular state and silicon diodes.

Due to its simplicity, the thermocouple is the most common temperature sensor used in the industry. Easy to use, with a rapid response to temperature change, small size, stability [10-12] and a temperature range from -2000C to + 26000C, thermocouple consists of two junctions of dissimilar metals joined at one end. The operating principle of the thermocouple is based on direct thermoelectric effect (Seebeck effect). It consists in the appearance of a

tensions termoelectromotoare in a closed circuit consisting of two different semiconductors when contacts are maintained at different temperatures.

Resistive temperature sensors are best suited to make accurate and repeatable temperature measurements. RTDs are manufactured from metals whose resistance increases with temperature. This resistance is directly proportional to the length of the metal wire and inversely proportional to the cross-sectional area and increases linearly with temperature. Made from high purity materials (platinum, copper, nickel), RTD's are temperature sensors with a precise and fast response [13]. Operating temperature range of RTD's is between -2000C to + 6000C.

The same mode of operation of the RTD's, thermistors are resistive temperature sensors manufactured from solid semiconductors [14] having a positive or negative temperature coefficient. Most used thermistors have a negative temperature coefficient (NTC) which means that the resistance value decreases with increasing temperature. Compared with RTD's and thermocouples, thermistors are weaker in construction and require more attention during installation to prevent crushing.

In the bimetallic devices, two metals with different thermal properties are soldered back to back. When heated, a part of the bimetallic strip deform more than the other. The main advantage of bimetallic devices is portability. Also, another advantage is independence from a power source. As disadvantage, the bimetallic devices are not accurate as the electronic devices. These devices are used in applications "ON / OFF" or "OFF / ON".

Specially manufactured for use in cryogenic temperature ranges, the silicon sensors have good conductivity and linearity in this temperature region. With increased robustness the silicon sensors are designed for repeatable measurements with good accuracy in temperature ranges between 1.4K and 500K [15]. This type of sensor is suitable for use in very high magnetic fields or in radiation medium [16].

Other important sensors are pressure sensors. A pressure sensor can generate an analog output proportional to pressure at it is or has a switching output operating at a predetermined pressure. Depending on the activity, the pressure sensors are classified as follows: vacuum sensors, sensors for medium pressure (10^2 Pa - 10^8 Pa) and sensors for high pressure ($> 10^8$ Pa) [17]. The most used sensitive elements to measure pressure are embedded diaphragm, plunger with spring, corrugated diaphragm, manometer open cell, closed cell manometer, biconical cell, bellows, Bourdon tube, twisted helical tube, one-eyed tube. The high pressures are measured using the following conversion types: piezoelectric effect and electromechanical oscillator. Sensors that use piezoelectric principle have the advantage of being robust, dynamic and with a response time of milliseconds. Stability and high precision sensors show using electromechanical oscillator principle but require numerical corrections which involve a microprocessor.

Major problems arise when desired to measure the cryogenic or high temperatures at very high pressures. These problems occur due to changes in the properties of materials used in sealing systems. Using sensors that require removal of supply wires and / or of output signals makes it difficult to seal the system and increase the cost of production. The temperature and pressure measurement in hazardous areas is also a problem. A solution to these problems would be to use optical detection sensors. Thus, the problems to sealing wires or the need to introduce the energized wires in explosive environments disappear.

Decrease energy consumption and miniaturization are other requirements of the consumer market. All these requirements and problems can only be solved by developing new materials with significantly improved physical properties. Materials with spin transition (ST), due to the physical differences between their two states, such as different colors, different volume or different electrical conductivity, have captured the attention of many research

groups and large companies involved in research. The ever growing interest in these materials is due to their high applicability potential in areas such as temperature and/or pressure sensors, information storage, micro switches and displays.

The purpose of this thesis is to offer new insight regarding the spin transition phenomenon from both points of view theoretical and experimental. Thus, in the first section of **Chapter 1** an introduction in SCO materials and the main perturbation factors that induce the spin transition is presented. In the second part of this chapter the main models and techniques used in characterization of behaviors of these interesting materials are presented.

In **Chapter 2** we describe the behaviors of some SCO compounds and their optical properties in the HS and LS states. So, taking into account the different colors of the two states, in the second part of this chapter, new proposed types of sensors involving SCO compounds, are presented. To understand how the behavior can be influenced by the external perturbation factors, architecture or internal interactions, in **Chapter 3**, using the Ising like model [18-20], a theoretical study concerning of these main factors that determine the evolution of SCO behavior is presented. Also, in this chapters, the influence of short and long interactions together with the architecture effect are studied. A new term is introduced in order to account for the interaction of edge molecules with their local environment and simulations were performed to investigate the influence of temperature and pressure.

In **Chapter 4**, using the Atom-phonon coupling model a theoretical analysis of spin crossover nanochains using a parabolic approximation was performed. It is well known that, apart from the system's cooperativity, which influences the hysteretic behavior of SCO complexes, the size of the system also plays a determinant role. The properties of the system are analyzed using a parabolic algorithm as a new method proposed in order to take into account the phonon contribution. Based on exact calculations, this method is more realistic and more efficient than the mean-field approximation (MFA). In particular, both the parabolic algorithm and the dynamic-matrix method are tested and compared and the analysis of the system's behavior shows that large size systems can be treated without generating all the system states. We also analyzed the role of degeneracy, and the thermal variation of both the entropy and heat capacity in the ferromagnetic-like coupling case. These studies play an important role in the choice process of SCO compounds for the desired application.

To highlight the temperature and pressure influence on SCO behavior, in **Chapter 5** we present an experimental analysis of $[\text{Fe}(\text{hyptrz})]_2\text{A}_2\cdot\text{H}_2\text{O}$ and $[\text{Fe}(\text{hyetrz})_3]_2\cdot\text{H}_2\text{O}$ SCO compounds. If for first compound a gas pressure cell was used to illustrate the thermal behavior at different pressures, for the second compound a home-made micromechanical device was used to analyze the pressure influence. The study is accompanied by a theoretical study in the framework of the Ising-like model allowing us to predict the bistability region of these two SCO compounds pertaining to sensor applications. In the end of this chapter, a new type of sensor involving two SCO compounds is proposed. This type of sensor is able to simultaneously indicate both temperature and pressure at which it is. It is very important to mention that for the fabrication of this sensor type, two SCO materials that exhibit a gradual transition without hysteresis are required.

The manuscript ends with general conclusions and perspectives.

1 State of the art

1.1 Introduction

Sensors market growth is a consequence of the ongoing development of new equipment and devices that must meet the increasingly stringent requirements of the end user. From miniaturization, multi-functionality and low power consumption, to applications that require high performance computing are some of the criteria in mind of the user when purchasing the desired product. Size reduction of electronic components has led to an increase in production costs due to the expensive equipment and costly components used in production. This is one of the reasons why, in recent years, miniaturization of electronic components reached the economic limit due to production costs. This is associated with the limiting issue in the miniaturization of components due to physical phenomena that occur when the material reaches a critical minimum size. Continuous technological development has led many research groups, including physicists, chemists and engineers, as well as companies to develop new materials with far superior physical properties which can be controlled at the molecular level [21-24]. Implementation of these materials in devices at both the macroscopic level and at the single molecule one, can be done only after a deep comprehensive understanding of the physical and chemical properties of the material. The use of these materials in the manufacturing process of electronic components should result in a reduction of the size of the components by orders of magnitude.

In this context, over the recent years, chemists have developed new techniques for the synthesis of molecular compounds with unique properties. An important category of multifunctional molecular compounds are the spin transition compounds (SCO) that attracted the attention of many research groups because of their potential applications [22,25-29]. First observed in the early 30s by L. Cambi and L. Szego, while studying the temperature dependence of magnetic susceptibility in molecular compounds containing Fe (III) ($3d^5$) centers [30], the phenomenon of spin transition (ST) was later discovered in other compounds containing metallic centers with $3d^4$ - $3d^7$ electronic configuration, such as: Fe (II) [31-33], Co (II) ($3d^7$) [34-37], Co (III) ($3d^6$) [38-40], Mn (II) ($3d^4$) [41,42], Mn (III) ($3d^5$) [43-46], Cr (II) ($3d^4$) [47-49]. These materials have a special particularity which is to switch between two stable magnetic states: a diamagnetic low spin state (LS) and a paramagnetic high spin state (HS). The two spin states are characterized by different physical properties such as different colors, different volumes or different electrical conductivities [22,50,51].

The most studied spin transition compounds so far have as a central ion Fe (II) in an octahedral configuration. The five orbitals of the Fe (II) ion are divided into two subsets [52,53]. A set consisting of t_{2g} (d_{xy} , d_{yz} , d_{zx}) orbitals and the second set consisting of two others e_g orbitals (d_{z^2} , $d_{x^2-y^2}$) with an energy higher than the t_{2g} orbitals energy (Figure 1.1).

Depending on the strength value of crystal field, represented by the energy gap of the levels t_{2g} and e_g , denoted by δ ($10Dq$) and the value of the electron pairing energy, Π , the six electrons can occupy the two different groups of orbitals, corresponding to the two following cases: (i) if the ligand field, δ is greater than the pairing energy, Π , $\delta > \Pi$, in violation of Hund's law, the electrons occupy the lowest energy orbitals, t_{2g} . In this case the sum of the spins is minimum ($S = 0$) and the compound will be in the LS state. For the second case, when $\delta < \Pi$ following Hund's law, electrons will occupy a number of orbitals as high as possible and the sum of the spins is maximum ($S = 2$), and the compound is in the HS state (Figure 1.2). The transition from one state to another is also characterized by a change in the volume of the molecule, due to the metal-ligand length change, this one being longer in the HS state than in the LS state. The spin transition phenomenon, represented by the transition

from one spin state to the other, occurs when the values of the two energies are approximately equal, $\delta \approx \Pi$.

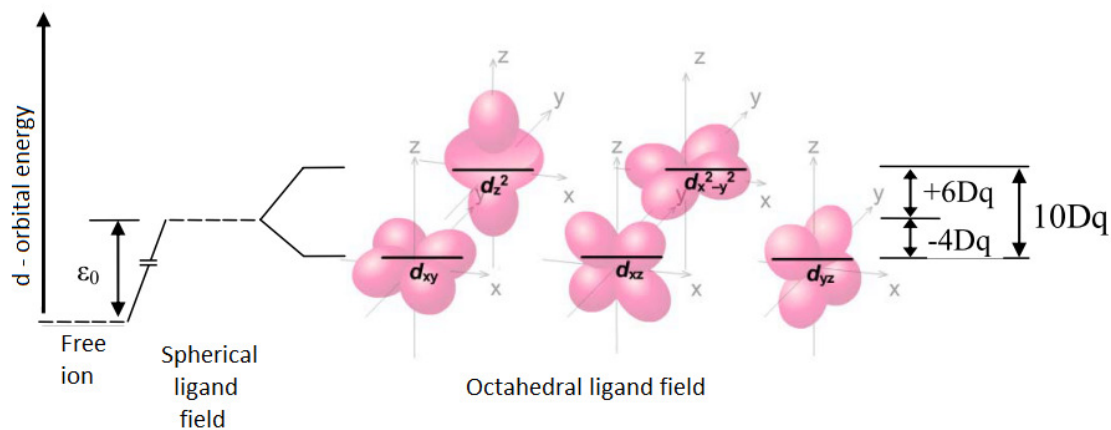


Figure 1.1 Representation of the five 3d orbitals.

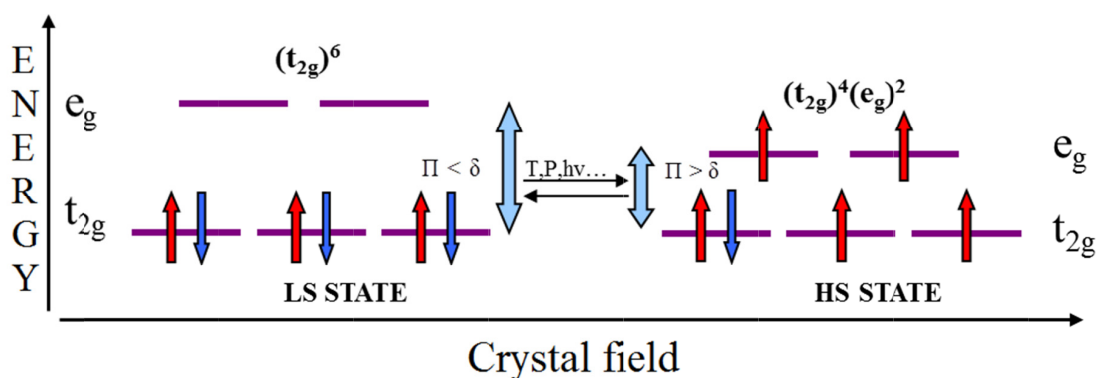


Figure 1.2 Electronic diagram of the HS and LS state for a Fe(II) ion in an octahedral ligand field.

Thus, under the action of external stimuli (temperature variation, pressure variation, applied magnetic or electric fields [22,54-56], light irradiation, etc.), the transition occurs between the diamagnetic LS state and the paramagnetic HS state or vice versa and is typically accompanied by significant changes in color, volume, magnetic state or electrical conductivity of the compound. These changes in physical properties can be observed using different characterization techniques such as: magnetic susceptibility measurements [33,57,58], Mossbauer spectroscopy [59], X-Ray diffraction [60-62], infrared and UV-vis spectroscopy [63,64] Raman spectroscopy [65], calorimetry [66-68], diffuse reflectance [27,69-71], ellipsometry [72,73] or optical microscopy [74].

1.2 The spin transition induced by temperature

One of the most used physical perturbations in order to induce the spin transition is the temperature. Depending on the type and intensity of the interactions between molecules, spin transition compounds may show different magnetic behavior with temperature variation (Figure 1.3): gradual or abrupt [75], two [76-80] or multi-steps [81-83], complete or incomplete [68,84] transitions, with or without hysteresis.

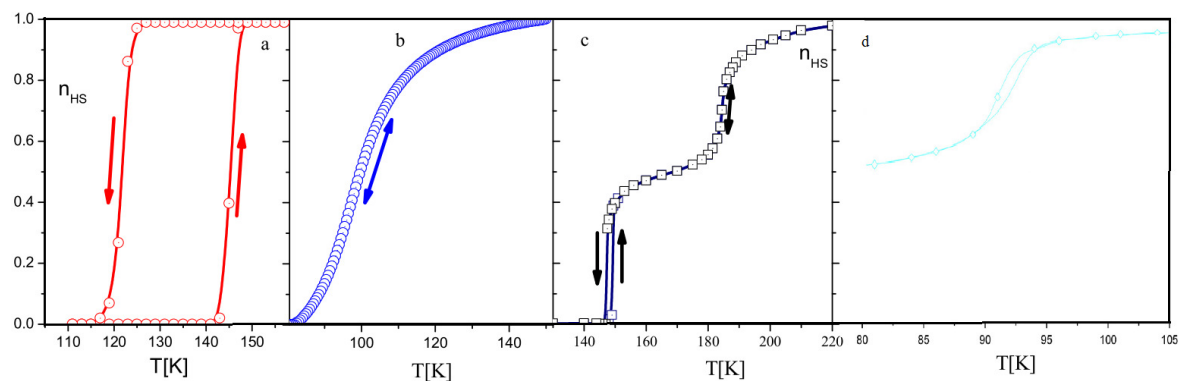


Figure 1.3 Various types of thermal induced spin transition: a) with hysteresis, b) gradual, c) two steps transition, d) incomplete [84,85]

1.3 The spin transition induced by pressure

A second main external perturbation that has been used to induce the spin transition is the application of an external pressure. From Figure 1.4 it can be seen that, by increasing the applied pressure the metal-ligand distance decreases resulting in the increase of the ligand field energy, Δ , and a decrease in the activation energy E_a . The transition from the LS state to the HS state occurs when the ligand field energy becomes greater than the energy of electron pairing. By applying an external pressure the volume of the molecule is decreased thus favoring the LS state.

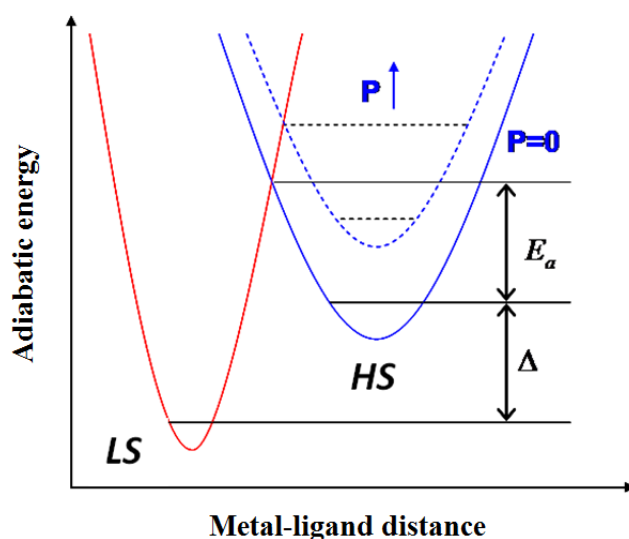


Figure 1.4 Schematic representation of the pressure influence.

1.4 Theory. Models and methods

In parallel with the various and numerous investigations on CTS, the need for describing and understanding the phenomena and processes occurring under the action of various external stimuli has led to the development of theoretical models and simulation methods regarding CTS behavior [86]. Proposed in the early 70s [18,87], the Wajnflasz and Pick model is the first one to introduce the concept of molecular interaction. This model is able to qualitatively simulate the temperature induced spin transition. The model introduces a fictitious spin with the eigen values $\sigma = 1$ (HS) and $\sigma = -1$ (LS). The interactions between the neighboring centers are described by an Ising type term, J . The total Hamiltonian is resolved by using mean field approximation and by taking into account the interactions with first order neighboring molecules only. Intermolecular interactions are not considered in this model.

In 1972, Bari and Sivardiere [88] continued the study by emphasizing some of the physical aspects that were ignored by the model of Wajnflasz et al., such as the temperature dependence of the intensity of the interactions. However, both models have a disadvantage concerning the entropy of the system associated with the two states (HS and LS) which does not show changes in the vicinity of the transition point which is a major issue [89].

The first model proposed to describe the influence of an applied external pressure on the spin transition behaviour is the Slichter and Drickamer model, developed in 1972 [90]. This model is the first to take into account the intermolecular interactions and, for years, has been the basis for other proposed models in order to point out the origin of interactions such as the atom-phonon coupling model or the mechano-elastic model. An important aspect is that this model entails a system of randomly distributed molecules, each molecule having its spin state independent of that of the neighboring molecule with which it interacts. Using this model and taking into account the intensity of interactions represented by the term T , both gradual transitions and step like transitions with and without hysteresis could be reproduced.

The model proposed by Sorai and Seki [91] in 1974 considered that the same spin state molecules are organized into independent domains. Their critical size can be calculated using calorimetric measurements. This model has the disadvantage that it cannot reproduce transitions with hysteresis.

1.4.1 Ising-like model

This model aims at providing a simple representation of the molecular states and intermolecular interactions. Starting with the model of Wajnflasz and Pick, the Ising-like model is adapted as a model with two different degenerate levels, each corresponding to a certain electronic configuration. If we consider that the molecules do not interact, the Ising type Hamiltonian of a system with two states, HS and LS, can be represented by the expression:

$$H = \frac{\Delta - k_B T \ln g}{2} \sum_{i=1}^N \sigma_i \quad (1.1)$$

where Δ is the energy difference between the two states, N is the number of molecules that compose the system, k_B is the Boltzmann's constant, T is the temperature of the system and σ_i is an operator associated to each molecule and that can take the value $+1$ when the molecule is in the HS state and the value -1 when the molecule is in the LS state. $g = g_{HS} / g_{LS}$ is the degeneracy ratio of the two states.

The spin fraction corresponding of the HS state is given by:

$$n_{HS} = \frac{1 + \langle \sigma \rangle}{2} \quad (1.2)$$

The equilibrium temperature of the system for which $n_{HS} = n_{LS} = 1/2$ corresponding to a zero effective field is given by:

$$T_{1/2} = \frac{\Delta}{k_B \ln g} \quad (1.3)$$

For a system of N interacting molecules, where the intensity of the interactions is being represented by the parameter value J , the system Hamiltonian has the following expression:

$$H = \frac{\Delta - k_B T \ln g}{2} \sum_{i=1}^N \sigma_i - J \sum_{\langle i,j \rangle} \sigma_i \sigma_j \quad (1.4)$$

Using this model, Bousseksou *et al.* [19] reproduced a two step transition considering two anti-ferromagnetically coupled molecular networks and, a few years later, the effect of intramolecular vibrations have been also taken into account [92]. In 1999 Linares *et al.* [20] reproduced, for the first time, the hysteretic transition of a 1D system considering the long-range interactions. Taking into account the long-range interactions, the Hamiltonian of the system can be written as:

$$H = \frac{\Delta - k_B T \ln g}{2} \sum_{i=1}^N \sigma_i - J \sum_{\langle i,j \rangle} \sigma_i \sigma_j - G \langle \sigma \rangle \sum_{i=1}^N \sigma_i \quad (1.5)$$

1.4.2 Atom phonon coupling model

Introduced in 2001 by Nasser [93] this model aims at providing an insight into the physical origin of intermolecular interactions in 1D systems. In this model molecules are modeled as atoms interconnected to each other through springs with a spring constant that depends on the electronic state of the molecules. The force between two neighboring interacting atoms i and j has an associated elastic constant k_{ij} given by:

- ✓ $C_{LL} = \lambda$, if the atoms are in the LS state ;
- ✓ $C_{HH} = \nu$, if the atoms are in the HS state ;
- ✓ $C_{HL} = \mu$, if an atom is in the LS state and other in HS state.

where $\lambda > \mu > \nu$.

Monte Carlo methods

Simulation of physical processes is a challenge for scientists trying to understand the physical phenomena that occur inside the materials. Thus, besides some analytical methods which can solve exactly finite or infinite systems, several other methods, mainly numerical have been developed. Monte Carlo methods are the most used methods by researchers in order to model probabilistic or stochastic systems whose analytical solutions are too complicated or impossible to be determined. Concerning SCO materials, the Monte Carlo methods are used in combination with certain models such as: Ising-like model, atom-phonon coupling (APC) model or mechano-elastic model. All these models are used by researchers to simulate the behavior of SCO materials when they are disturbed by an external perturbation such as: thermal or/and pressure variation, light irradiation, applied magnetic or electrical fields.

1.4.3 Monte Carlo Metropolis

This method introduced by Metropolis [94] was initially proposed for the specific case of a canonical ensemble but it has been adopted in other fields. The Metropolis algorithm consists in the following description: a system with a configuration C_i of spin operators and

with energy E_i is shifted in the configuration C_{i+1} with energy E_{i+1} by changing a spin operator, k , from its initial value σ_k to $-\sigma_k$ only if the following conditions are met: (i) the energy of the new configuration is lower than the previous one or (ii) in the opposite case, then a random number, R is generated, in the interval $[0,1]$; if the probability to move from the configuration C_i to configuration C_{i+1} , $P = e^{-(E_{i+1}-E_i)/k_B T}$, is less than the value of R , the new configuration is accepted. Otherwise, the new configuration is refused and restarting from the same configuration C_i , the same steps are applied. This new configuration will be accepted or not depending on the fulfillment of the conditions specified above.

This method has been used over the years in combination with main models that are used to describe the spin transition behavior [95-97].

1.4.4 Monte Carlo entropic sampling

The Monte Carlo Entropic Sampling (MCES) can be used when the Hamiltonian of the system cannot be solved exactly via the transfer matrix method or when the mean-field approximation method is not appropriate enough for researchers' investigations. The MCES in combination with the Ising-like model is used to obtain the table that contains the macroscopic variables, m and s , and their density, $d(m,s)$, m and s are defined as:

$$m = \sum_{i=1}^N \sigma_i \quad \text{and} \quad s = \sum_{\langle i,j \rangle} \sigma_i \sigma_j \quad (1.6)$$

The principle of MCES, described by the Shteto et al. [98,99] is the follow: in order to obtain a desired distribution P , it is necessary to introduce an appropriate distribution as a bias in the detailed balance equation expressed as:

$$P_i W(i \rightarrow j) = P_j W(j \rightarrow i) \quad (1.7)$$

The biasing probability was chosen as the inverse of the desired restricted density of states.

$$P_i \propto \frac{1}{d(m_i, s_i)} \quad (1.8)$$

In this way, configurations with weakly degenerate macrostates are favored and those with highly degenerate states are damped. In this case, the balance equation (1.7) can be written as:

$$\frac{W(i \rightarrow j)}{W(j \rightarrow i)} = \frac{P_j}{P_i} = \frac{d(m_i, s_i)}{d(m_j, s_j)} \quad (1.9)$$

Because in the first Monte Carlo step the density of the state $d(m,s)$ is unknown we put all $d(m,s)$ equal to 1. So, after iteration k the density will be $d_k(m,s)$. Then, using $d_k(m,s)$ as a bias, a MC sampling is run; it is termed a 'Monte Carlo stage' and yields a histogram of the frequency of the macrostates: $H_k(m,s)$:

$$H_k(m,s) \propto d(m,s) \frac{1}{d_k(m,s)} \quad (1.10)$$

The resulting restricted density of states is obtained after applying a correction for the bias:

$$d_{k+1}(m,s) \propto d_k(m,s) H_k(m,s) \quad (1.11)$$

From the table of the $d(m,s)$ thus built from the (m, s) states, the partition function can be calculated using the following expression:

$$Z = \sum_{(m,s)} d(m,s) \exp(-\beta(-hm - Js)) \quad (1.12)$$

from which all the thermodynamic properties of the system can be analytically derived.

So, in the evolution of the HS fraction given by equation (1.2) the average magnetization can be written as:

$$\langle \sigma \rangle = \frac{\sum_{i=1, NL} \frac{m_i}{N} d(m_i, s_i) \exp\left(-\frac{1}{k_B T} (-h_f m_i - J s_i)\right)}{\sum_{i=1, NL} d(m_i, s_i) \exp\left(-\frac{1}{k_B T} (-h_f m_i - J s_i)\right)} \quad (1.13)$$

where NL is the number of distinct configuration of states $\langle m, s \rangle$ and $d(m, s)$ is the number of configuration for a given set of values.

2 Sensing applications of SCO materials

2.1 Introduction

Variation of temperature and/or pressure is most often used to induce the spin transition phenomenon. In this chapter the behaviors of a few compounds and their colors in both LS and HS spin states, respectively are presented. The potential applications as sensors of these materials are also presented in this chapter.

The temperature and pressure effects have been extensively studied in terms of both experimental and theoretical standpoint. In order to experimentally investigate simultaneous the temperature and pressure effect of SCO compounds, a pressure cell, connected to a high pressure system, was been used. Due to the color change of these materials in response to a temperature and/or pressure change, SCO materials are considered to be good candidates for practical implementation as temperature or pressure sensors.

2.2 Temperature sensors

Over the years have been reports of SCO materials exhibiting a strong color contrast between the two transitional states (Figure 2.1). Thus, as a result of temperature and/or pressure variations, different behaviors of spin transition compounds have been reported.

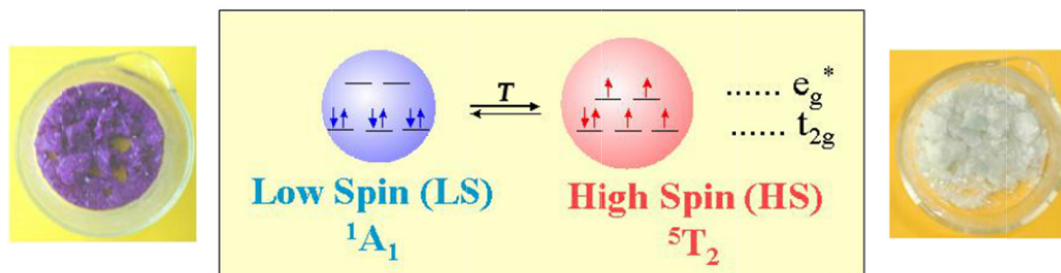


Figure 2.1 The color changes and electron distribution of Fe(II) in the LS and HS states. [100]

The fascinating behavior of these materials has sparked the interest of many research groups. Thus, in 2006, Seredyuk et al [101] reported on a liquid compound which exhibited a strong color contrast between the two states (Figure 2.2). They also showed that, with dehydration of the compound, the transition is more gradual and linear (Figure 2.3).

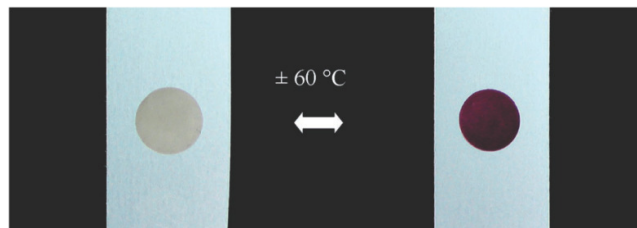


Figure 2.2 Change of color in the SCO liquid crystalline films around 60 °C of $[\text{Fe}(\text{C}_n\text{-trz})_3](4\text{-MeC}_6\text{H}_4\text{SO}_3)_2 \cdot \text{H}_2\text{O}$ [101].

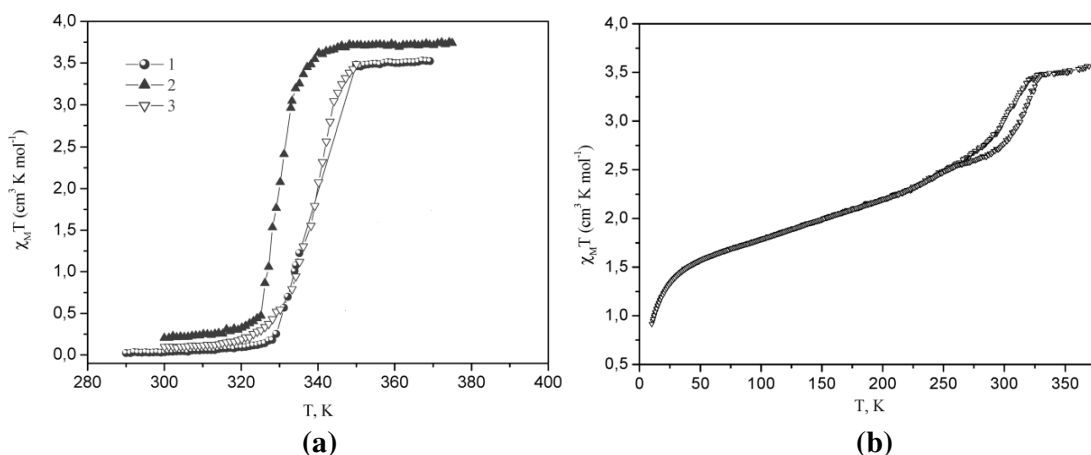


Figure 2.3 The thermal variation of magnetic properties of the complexes (a) $[\text{Fe}(\text{C}_n\text{-trz})_3](4\text{-MeC}_6\text{H}_4\text{SO}_3)_2 \cdot \text{H}_2\text{O}$ (for the cases 1 - $n=8$, 2 - $n=10$ and 3 - $n=12$) and (b) $[\text{Fe}(\text{C}_n\text{-trz})_3](4\text{-MeC}_6\text{H}_4\text{SO}_3)_2$ - $n=12$ [101].

Another interesting compound, exhibiting a great color contrast during the spin state switching, was synthesized by Coronado et al [102]. This compound has the great advantage of an increased stability over time (Figure 2.4a). The transition cycles in Figure 2.4a were measured on $[\text{Fe}(\text{Htrz})_2(\text{trz})](\text{BF}_4)$ particles of diameters around 10 nm, obtained by the use of the "micelle technique".

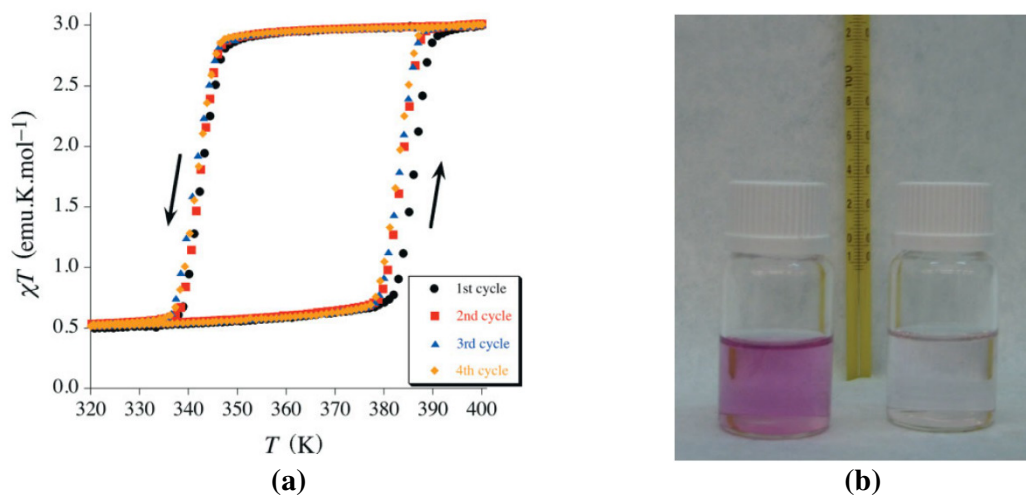


Figure 2.4 (a) Magnetic thermal hysteresis for compound $[\text{Fe}(\text{Htrz})_2(\text{trz})](\text{BF}_4)$; (b) The colors at room temperature in the low spin state (left) and the high spin state (right).

In Figure 2.5a) is presented a proof-of-concept experiment where a gold microwire ($L = 80\mu\text{m}$, $l = 1\mu\text{m}$, $h = 5\text{ nm}$) covered by a thin layer of SCO compound $[\text{Fe}^{\text{II}}(\text{hptrz})_3](\text{Ots})_2$ doped with Rhodamine 110 is heated by Joule effect [103]. The temperature distribution along the wire is presented in Figure 2.5b). The scheme of the device is shown in Figure 2.5 c). The temperature variation is a consequence of the luminescence intensity change. By increasing the temperature the spin state of the compound that cover the gold microwire will change locally from LS to HS state and the luminescence intensity will increase.

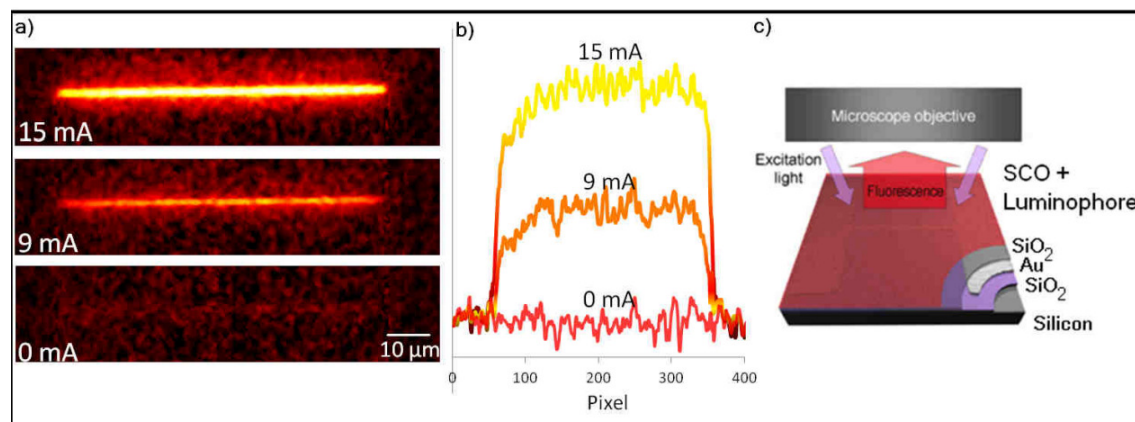


Figure 2.5 Example of sensor using SCO compounds [103]

2.3 Pressure sensors

The pressure effect on a spin transition compound is illustrated in Figure 2.6. It is well known that the molecule's volume in its LS state is smaller than in the HS state. Therefore the application of external pressure promotes the LS state. By applying an external pressure the energy gap increases by $p\Delta V$ as the metal-ligand distances decrease thus lowering the value of the activation energy E_a . ΔV is the molecular volume variation during the spin transition and p is the external applied pressure.

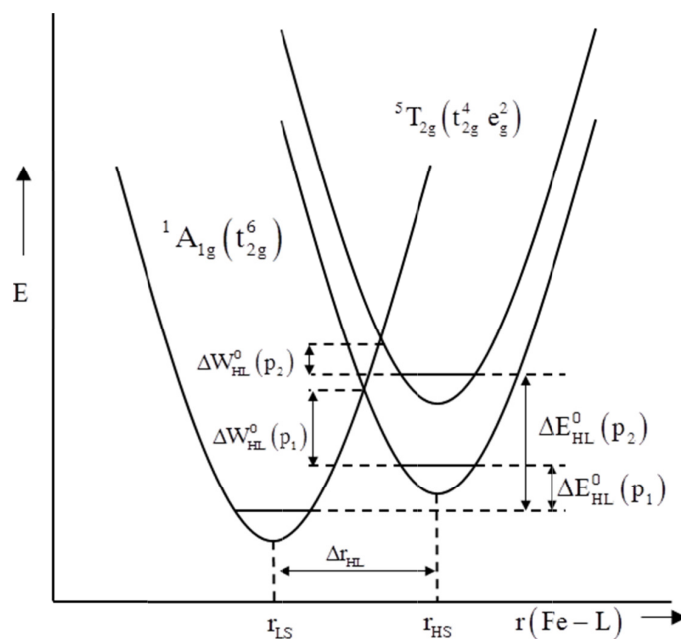


Figure 2.6 Schematic representation of the pressure influence on the LS and HS potential wells of an Fe(II) SCO compound [104].

As previous mentioned, the pressure dependence of the energy gap is given by:

$$\Delta(T, p) = \Delta(T, p = 0) + p\Delta V \quad (2.1)$$

Up until a few years ago the SCO compounds exhibiting a thermal hysteretic behavior were intensely studied due to potential application as memory. In the recent years the SCO compounds with gradual and linear transition drew attention of several research groups. This

type of behavior accompanied by color changes of the compound opened a new area of implementation, namely the sensors. In 2012 Linares et al. [25] proposed a concept of sensor based on SCO compound. The operating principle is shown in Figure 2.7.

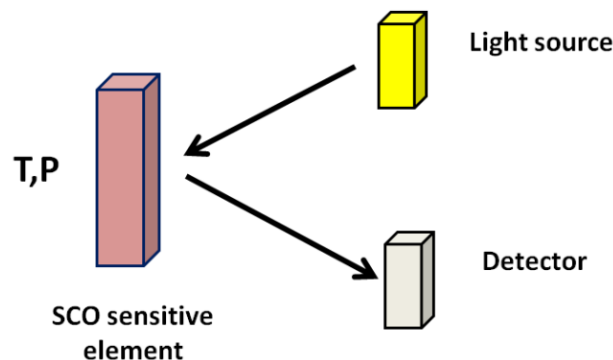


Figure 2.7 The operating principle of a SCO sensor with optical reflectivity detection [25].

This type of sensor can be used for temperature measurement at a well-known pressure or for pressure measurement at constant temperature. It is important to mention that the measurement error is estimated to c.a 20K/kbar rate variation of T vs P [105]. Thus, when the sensor is used for temperature measurement the 1bar variation of pressure induce an error of 20 mK. On the other hand, the pressure measuring can be done with an error of 50 bars at variation of temperature with 1 K. The contrast of the color change of the material plays also an important role in the sensitivity and resolution of measurement process. Using the advantages of these materials such as change in color, repeatability, time responding and the possibility to be controlled at molecular level, such kind of materials are being commercialized for various applications where a wide selection of colors (Figure 2.8) [106] is necessary.

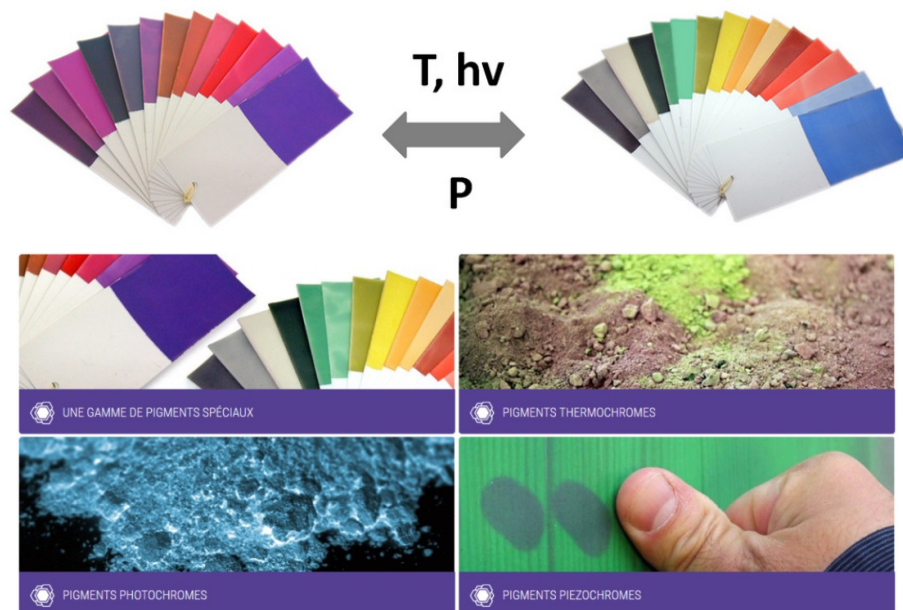


Figure 2.8 Types of pigments and their applications [106].

3 Cooperativity tuning in spin crossover nanostructures via matrix and architecture effect

3.1 Introduction

The role of cooperativity in SCO materials has attracted great interest from unusual observations revealed experimentally [18-20,25-27,40,76,82,107-115]. **The origin of cooperativity** is assigned to elastic interactions between neighboring switching molecules and as a function of the interaction strength among molecules and/or of the lattice architecture, the spin transition (ST) curve can display a variety of shapes which can be gradual, abrupt, or stepwise [53]. Increasing the strength of these interactions, the cooperative phenomena between the spin state changing molecules can lead to a hysteretic behavior. In the last years a special attention has been paid to the two-step behavior which was attributed to a synergistic effect between intra-molecular interactions favoring the mixed-spin state and intermolecular interactions favoring like-spin species domains. In the last five years, several coordination complexes have been shown to present a ST occurring in three steps [107-109]. Although the origin of the two-step behavior is rather clear, the origin of the three-step behavior is far from being fully understood. However, there is clear evidence that this stepwise behavior should be governed by both matrix (i.e. surface effect) and long-range interaction effects [83,116].

In the first part of this chapter, a theoretical study concerning the influence of an elastic environment on a SCO system is presented. By reducing the particle's size, the surface contribution became more important comparing with the bulk behaviour. Moreover, the fabrication of a temperature and pressure sensor with optical detection demands the integration of the SCO complexes in a matrix. This make very important to know how SCO behavior is influenced by the interaction of SCO molecules with their environment. Thus, the edge effect might play an important role on the spin crossover behavior. Indeed, it has been shown that the edge effect could led through a multi-step behavior. This kind of behavior has been experimentally observed in 2D and 3D SCO systems [107-109] but not yet for 1D systems. We used Ising-like model [18-20] in order to simulate the edge effect in SCO systems. These studies are very important for engineers in the fabrication process of temperature and pressure sensors.

In the second part of the chapter is analyzed the architecture effect of a SCO system.

3.2 Matrix effect on spin crossover nanoparticles on the origin of multi-step spin transition behavior in 1D nanoparticles

3.2.1 The Ising-like model with edge effect

It is known that the SCO compounds that exhibit hysteresis can be used as memories and those whose transition is gradual can be used as sensors. Thus, compounds with gradual transition can be obtained by synthesis or may be diluted compounds that exhibit transition with hysteresis. By dilution the system cooperativity is reduced and can appear new interactions if the compounds are mixed for example with paints. In order to take into account these new interactions (the matrix effect), we have added an additional interaction parameter to the Ising-like Hamiltonian [20] which accounts for the SCO molecules behavior within the environment (matrix effect), that is termed, the matrix interaction L . This interaction is assumed to act on the molecules localized at both ends of the 1D SCO system. In this case, the system's Hamiltonian can be written as follows:

$$H = \frac{\Delta - k_B T \ln g}{2} \sum_{i=1}^N \sigma_i - G \sum_{i=1}^N \sigma_i \langle \sigma \rangle - J \sum_{\langle i,j \rangle} \sigma_i \sigma_j - L \sum_{\{i=1, i=N\}} \sigma_i, \quad (3.1)$$

where the first term represents the temperature dependent field, the second and third terms are describing the long- and short-range interactions, respectively. The last term describes the interaction of the SCO system with the matrix. Δ is the energy gap between the high-spin (HS) and low-spin (LS) states, and g is the degeneracy ratio of the two states.

Since the ratio of HS state n_{HS} as a function of the pseudo-spin variable can be expressed by:

$$n_{HS} = (1 + \langle \sigma \rangle) / 2 \quad (3.2)$$

and appears self-dependent of $\langle \sigma \rangle$, we propose an analytical treatment using a new expression of n_{HS} based on the bisection technique.

Thus, the system's Hamiltonian could be expressed as a function of the dimensionless macroscopic variables:

$$m = \sum_{j=1,N} \sigma_j \quad (3.3)$$

$$s = \sum_{\langle i,j \rangle} \sigma_i \sigma_j \quad \text{and} \quad (3.4)$$

$$c = \langle \sigma_1 + \sigma_N \rangle \quad (3.5)$$

(herein σ_1 and σ_N represent the spin operator associated to the first and the last molecule in the molecular chain):

$$H = \left(\frac{\Delta - k_B T \ln g}{2} - G \langle \sigma \rangle \right) m - Js - Lc \quad (3.6)$$

The canonical expression of $\langle \sigma \rangle$ can be constructed in terms of the above dimensionless quantities:

$$\langle \sigma \rangle = \frac{\sum_{j=1,NL} \frac{m_j}{N} d(m_j, s_j, c_j) \exp\left(-\frac{1}{k_B T} (-h_j m_j - Js_j - Lc_j)\right)}{\sum_{j=1,NL} d(m_j, s_j, c_j) \exp\left(-\frac{1}{k_B T} (-h_j m_j - Js_j - Lc_j)\right)} \quad (3.7)$$

where $d(m, s, c)$ is the number of configurations for a given set of values, NL is the number of distinct configurations of states $\langle m, s, c \rangle$ and where:

$$h_f = -\left(\frac{\Delta - k_B T \ln g}{2} - G \langle \sigma \rangle \right) \quad (3.8)$$

Since $d(m, s, c)$ is the degeneracy of each state $\langle m, s, c \rangle$, we are able to generate all the system configurations building by this way, the states distributions of the molecular system.

Upon considering open boundary conditions and following the numerical calculation of equation (3.7) from the bisection technique, the curves from Figures 3.1 and 3.2 were obtained where n_{HS} is given by equation (3.2). Moreover we discuss in the rest of the study some simulations regarding the behavior of a 1D system using the values of parameters Δ , $\ln(g)$ in the range of those of SCO compounds.

In the numerical studies [81,82] it was shown that a stepwise behavior could be obtained in 3D SCO systems by taking into account negative short-range interactions (anti-ferromagnetic-like interactions) and positive long-range interactions (ferromagnetic-like interactions). Following similar conditions, it is further considered in this work, that the coupling between the matrix and the edge molecules is ferromagnetic-like (positive).

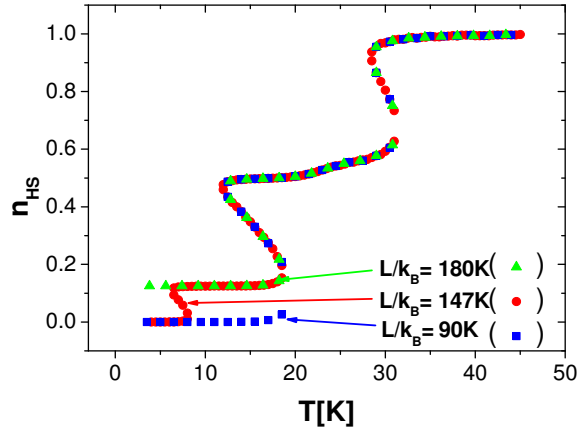


Figure 3.1 Thermal evolution of the HS molar fraction, n_{HS} , in a 1D SCO system embedded into a matrix for different matrix interaction strength: Square ($L/k_B = 90$ K), Circle ($L/k_B = 147$ K) and Triangle ($L/k_B = 180$ K). The parameter values are: $N = 16$ molecules, $\Delta/k_B = 240$ K, $\ln(g) = 9.5$, $G/k_B = 120$ K, and $J/k_B = -43$ K.

In figure 3.2, the simulated thermal behavior of the HS fraction is shown for various numbers of molecules. We show that, when the SCO system size consists of a high number of interacting molecules, the thermal behavior of the 1D SCO system, depending on the matrix interaction strength, can exhibit both two-step and three-step ST and both complete or incomplete transition. Another feature that was observed with the decrease of the number of molecules, is a shift of the equilibrium temperature $T_{1/2}$ to low temperatures, in good agreement with the experimental data reported in [117].

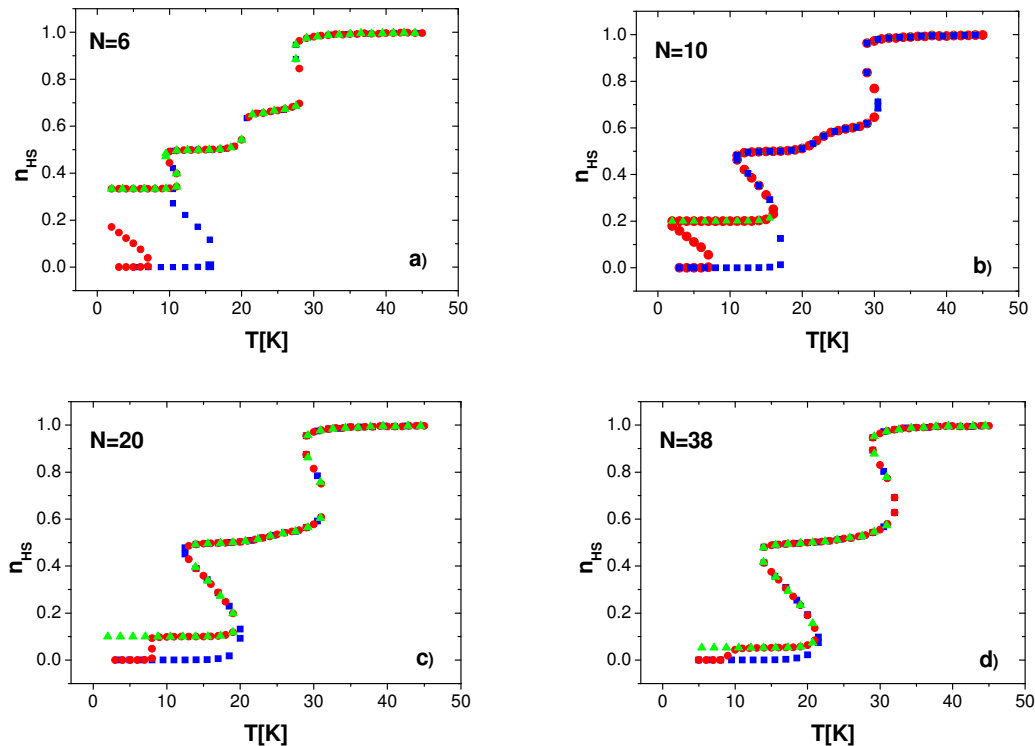


Figure 3.2 Evolution of the HS molar fraction, n_{HS} , as a function of temperature, for various numbers of molecules: (a) $N=6$ molecules, (b) $N=10$ molecules, (c) $N=20$ molecules, (d) $N=38$ molecules for different polymeric-interactions strength: Square ($L/k_B = 90$ K), Circle ($L/k_B = 147$ K) and Triangle ($L/k_B = 180$ K). The computational parameters are: $\Delta/k_B = 240$ K, $\ln(g) = 9.5$, $G/k_B = 120$ K, and $J/k_B = -43$ K.

In figure 3.3 we show the case where L as well as J , the short range interaction are 0, together with the case with $L/k_B = 147$ K and $J/k_B = -43$ K. It is clear from this figure that the multi-steps hysteresis transition originates from the interaction of the border SCO molecules with the local environment together with an antiferromagnetic-type short range interaction.

The value of the parameter L , which is a “long-range interaction” between the matrix and the SCO at the surface, is of the same order with the long-range interaction parameter G .

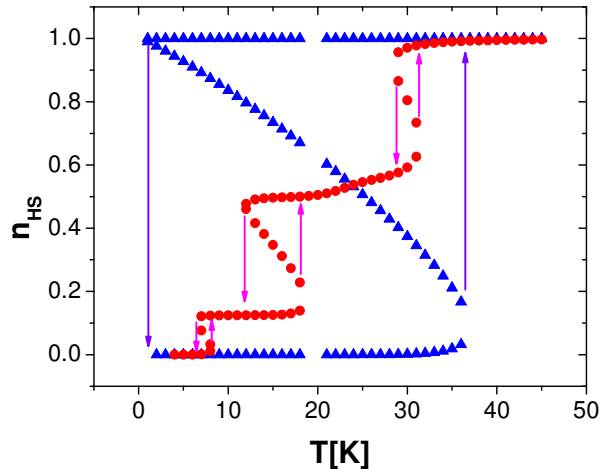


Figure 3.3 Evolution of the HS molar fraction n_{HS} as a function of temperature, for the case: (Circle) ($L/k_B = 147$ K, $J/k_B = -43$ K) and (Triangle) ($L/k_B = 0$ K, $J/k_B = 0$ K). The computational parameters are: $N=16$, $\Delta/k_B = 240$ K, $\ln(g) = 9.5$ and $G/k_B = 120$ K.

The role of the long-range (G), as well as the short-range interaction, on the thermal behavior are presented in figure 3.4 and figure 3.5 respectively. For a high value of the long-range interaction, three-step hysteretic behavior can be reproduced, however the hysteresis disappears, as we expected, for small values of the long-range interaction.

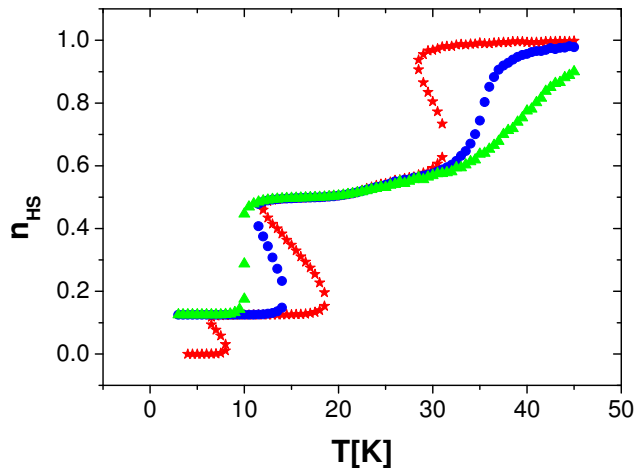


Figure 3.4 Evolution of molecules in the HS state, n_{HS} , as a function of temperature, for a 1D system $N= 16$ molecules, for different long range-interactions strength: $G/k_B = 40$ K (triangle), $G/k_B = 80$ K (circles), $G/k_B = 120$ K (star) The parameter values are $\Delta/k_B = 240$ K, $\ln(g) = 9.5$, $J/k_B = -43$ K, and $L/k_B = 147$ K.

The short-range interaction strength plays an important role on the stepwise behavior. Thus, when the short-range interaction strength dominates the other two interactions parameters, i.e. long-range and the matrix interaction parameters, the stepwise behavior is

more pronounced. For a small value of short-range interaction, the stepwise behavior can be masked by a macroscopic one-step behavior.

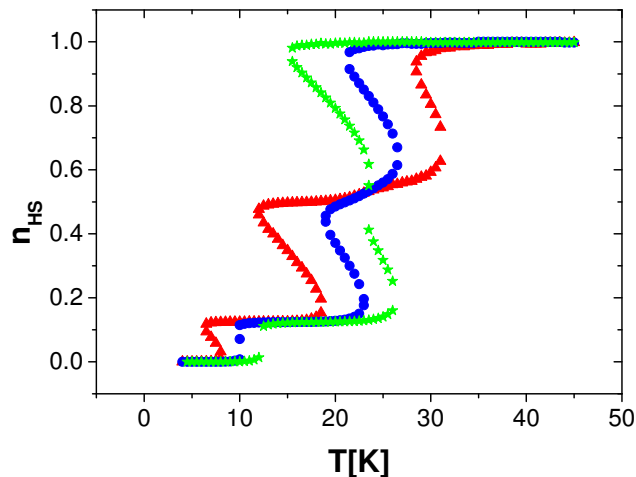


Figure 3.5 Evolution of molecules in the HS state, n_{HS} , as a function of temperature, for a 1D system $N=16$ molecules, for different long short-interactions strength: $J/k_B = -43$ K (triangle), $J/k_B = -30$ K (circle) and $J/k_B = -20$ K (star). The parameter values are $\Delta/k_B = 240$ K, $\ln(g) = 9.5$, $G/k_B = 120$ K, and $L/k_B = 147$ K.

3.3 Size dependence of the equilibrium temperature in 2D SCO system

Figure 3.6 illustrates the thermal behavior of the HS fraction, $n_{HS}(T)$, calculated for various particle sizes. Upon decreasing the particle size ($N_x \times N_x$), the transition temperature is shifted downward and the width of the thermal hysteresis loop progressively increases as a result of surface effects. The detailed discussion of the results of the model follows. This behavior contrasts with the classical behavior of the thermal hysteresis with particle size, for which it monotonously vanishes at small sizes.

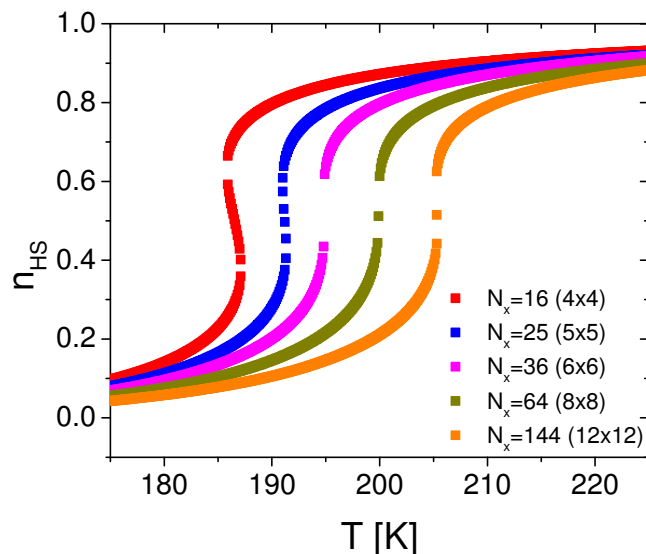


Figure 3.6 The simulated thermal behavior of the total HS fraction, $n_{HS}(T)$, for different system's sizes, showing an increase of the thermal hysteresis width for smaller nanoparticle sizes. The computational parameters are: $\Delta/k_B = 1300$ K, $G/k_B = 172.7$ K, $J/k_B = 15$ K, $L/k_B = 120$ K, $\ln(g) = 6.01$.

We could separate the contributions of surface atoms and core atoms in the thermal behavior of the total HS fraction of figure 3.6. Figure 3.7 displays two chosen cases of nanoparticles with sizes (4x4) and (12x12) depicting all contributions. One can clearly see, that in both cases, the surface (blue curves) starts to transform much earlier than the core (green curves), which clearly indicates that the surface is driving the thermal LS to HS transitions. It is however obvious that for very bigger sizes (unreachable with MCES method), the contribution of the surface will be marginal and the core will dominate. This tendency is already visible in the case of 12x12 particle, in which we remark that the curve of the total response (red) is much closer to that of the bulky atoms.

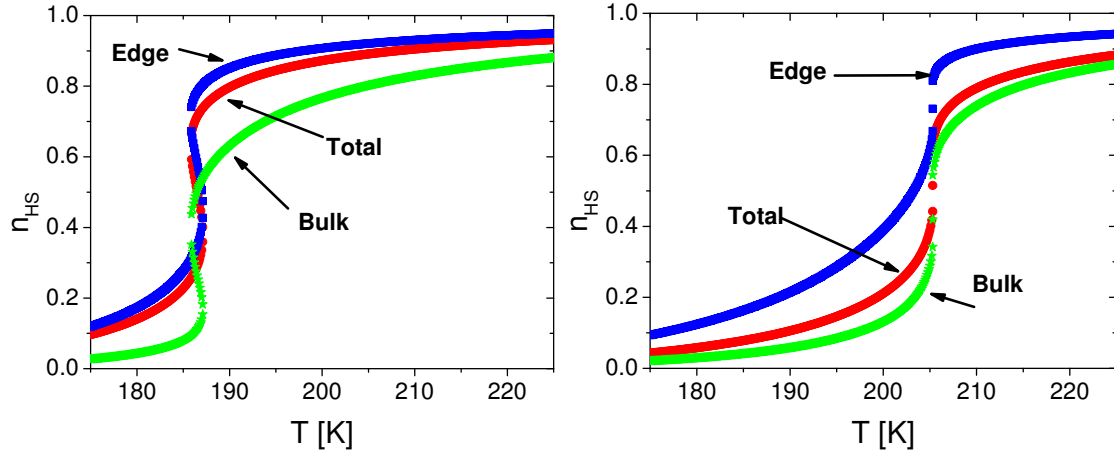


Figure 3.7 The thermal behavior for the edge, inner and total molecules of the system for the cases: left - $N_t = 16$ (4x4) and right - $N_t = 144$ (12x12). The model parameters are the same as those of Figure 3.6.

We found that the size dependence of the transition temperature could be described by analytical laws (easily extended to 3D models). Here, it worth mentioning that even for small sizes, exact analytical solutions of Hamiltonian (1) in 2D are out of reach [118], contrary to our previous studied case where the surface atoms were fixed in the HS state [119].

We introduce here a simple idea that the transition temperature of the system is still the result of a null total effective ligand-field. From the expressions of the ligand field for the edges and core atoms, as listed in Table 3.1, the transition temperature, T_{eq} , for a square lattice $N_x \times N_x$ is the solution of the following equation:

$$\frac{\Delta - k_B T_{eq} \ln g}{2} \times (N_x - 2)^2 + \frac{\Delta - 2L - k_B T_{eq} \ln g}{2} \times 4(N_x - 1) = 0 \quad (3.9)$$

which expresses that the total ligand-field is equal to zero at $T = T_{eq}$.

	Total	Edges	Core
Number of atoms	N_x^2	$4(N_x - 1)$	$(N_x - 2)^2$
Ligand-field		$\frac{\Delta - 2L - k_B T \ln g}{2}$	$\frac{\Delta - k_B T \ln g}{2}$

Table 3.1. The ligand-field correlated to the molecules number.

Solving equation (3.9) gives the analytical expression of the lattice size-dependence of the transition temperature, as:

$$T_{eq} = \frac{N_c}{N_t} T_{eq}^{bulk} + \frac{N_s}{N_t} T_{eq}^{surf}, \quad (3.10)$$

which for a 2D square system can be written as:

$$N_x^2 T_{eq} = (N_x - 2)^2 T_{eq}^{bulk} + 4(N_x - 1) T_{eq}^{surf}, \quad (3.11)$$

leading to a parabolic and linear contribution of the bulk and surface contribution to $N_x^2 T_{eq}$ respectively.

In equation 2.12, T_{eq}^{bulk} and T_{eq}^{surf} are the transition temperatures of the bulk and the surface, whose expressions are:

$$T_{eq}^{bulk} = \frac{\Delta}{k_B \ln g} \approx 216.3K \quad \text{and} \quad T_{eq}^{surf} = \frac{\Delta - 2L}{k_B \ln g} \approx 176.3K \quad (3.12)$$

Equation (3.10) predicts that the transition temperature has two limiting values, namely $T_{eq} = T_{eq}^{surf} = 176.3K$ for $N_x = 2$ for the smallest nanoparticle size, and $T_{eq} = \frac{\Delta}{k_B \ln g} \approx 216K$ corresponding to the bulk transition temperature, reached for an infinite lattice ($N_x \rightarrow \infty$).

3.4 Analysis of edge effect in 3D systems

3.4.1 Results and discussions

In this study, we first consider a 3D SCO system whose edge metallic centers interact with its environment and apply the bisection technique to equation (3.7). The HS fraction, n_{HS} , is derived from equation (3.2). The SCO selected system contains 125 metallic centers (5x5x5) of which 98 are surface metallic centers and only 27 are inner metallic centers. A typical distance between metal centers of about 9 Å [58] is taken into account corresponding to a cubic sampling of 3.6 nm x 3.6 nm x 3.6 nm. As a result, a hysteretic multi-steps transition is predicted (figure 3.8).

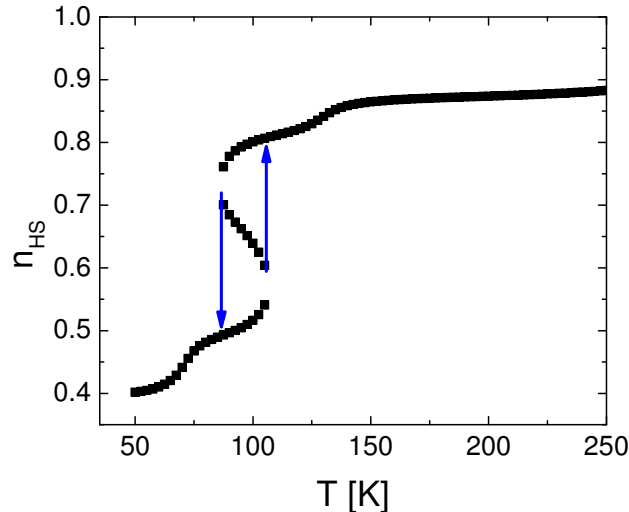


Figure 3.8 Simulated HS fraction, n_{HS} , as a function of temperature for a 3D SCO system. The computational parameters are $N = 125$ (5x5x5), $\Delta/k_B = 1450K$, $G/k_B = 470K$, $J/k_B = -100K$, $L/k_B = 750K$ and $\ln(g) = 4.7$.

For comparison purposes, we plotted the computed thermal behavior without edge effect on figure 3.9. The following conclusions can be drawn: (i) the hysteresis related to the middle-step disappears, (ii) the HS fraction increases from 0 (when $L/k_B = 0K$) to 0.4 (when

$L/k_B = 750$ K), (iii) the transition is shifted to lower temperatures, which means that the edge interaction seems to have an action opposite to a typical applied pressure because the edge interaction favors the HS state while an applied pressure is known to favor the LS state, due to its lower ionic volume.

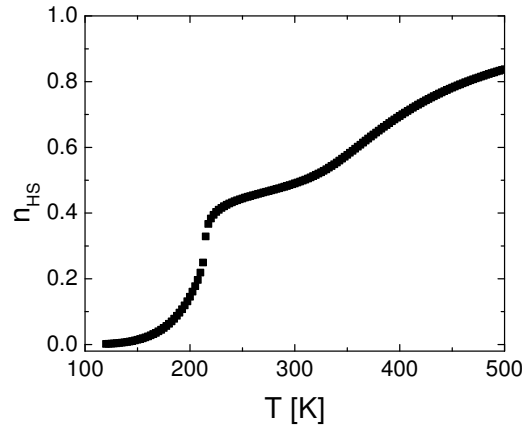


Figure 3.9 Simulated HS fraction, n_{HS} , as a function of temperature for a 3D SCO system when $L/k_B = 0$ K. The other parameters are the same as those of figure 3.8.

Finally, we have investigated the increase of the system's size (figure 3.10). By increasing the system's size, i.e. by decreasing the ratio between edge and inner metallic centers (from 7 for a cube system with 64 metallic centers to 3.629 for a system with 125 metallic centers and to 2.375 for a system with 216 metallic centers), the edge effect decreases and the role of inner metallic centers increases. As a result, when we increase the size of the system, the equilibrium temperature, $T_{1/2}$, is shifted to higher temperatures and the transition proceeds continuously from the LS state to the HS state.

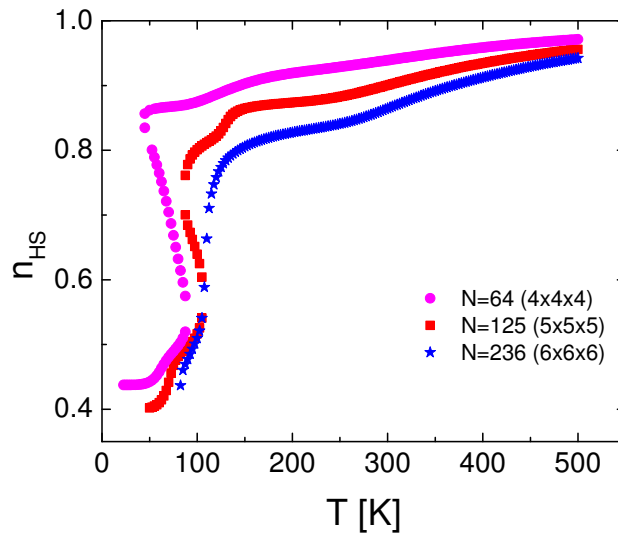


Figure 3.10 Simulated HS fraction, n_{HS} , as a function of temperature for 3D SCO systems of different sizes. Other parameters are the same as those of figure 3.8.

3.5 Analysis of architecture effect

In the beginning of this subsection, the hysteretic properties of thermal induced LS \leftrightarrow HS phase transition of a 3D SCO nanostructure is analyzed when the cluster architecture is progressively changed from a cubic to a thin film. For this study the edge molecules was considered blocked in the HS state. The second part is dedicated to the study of architecture

effect in a 2D SCO system when the edge molecules are considered as active molecules that interact with their local environment.

The study of architecture effect for 1D and 2D SCO systems reported in [120] shows that the 1D system exhibits a gradual transition for a weak cooperativity system or a thermal transition for a strong value of short range interaction. For 1D ladder type systems the transition occurs with hysteresis and the hysteresis width increases more for a 2D square system (figure 3.11).

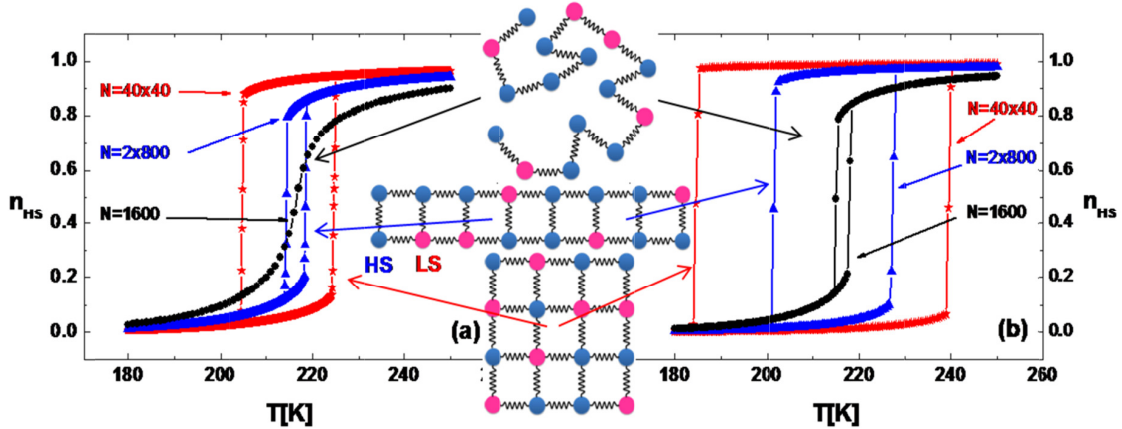


Figure 3.11 Evolution of HS fraction for different architectures of systems for the cases (a) $J/k_B=64K$ and (b) $J/k_B=105K$. The computational parameters are: $\Delta/k_B=1300K$, $\ln(g)=6$, $G/k_B=105K$ [120].

Up to now, there are few numerical studies of surface and architecture effects on the hysteretic behavior of nanostructured SCO system, since experimental work is also rather recent.

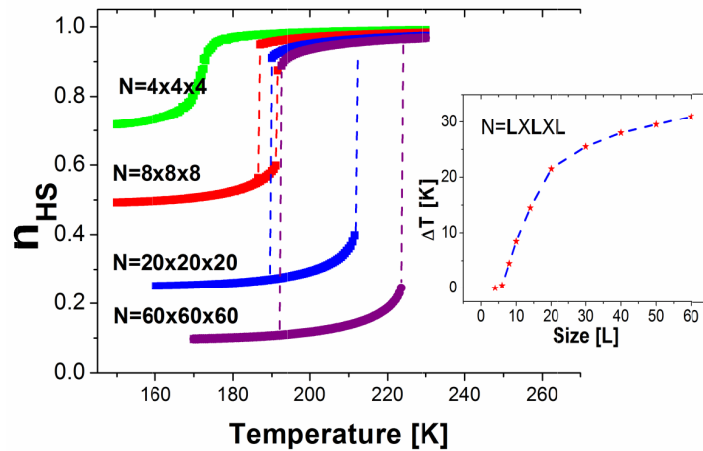


Figure 3.12 Simulated thermal transition for different sizes of a cubic system. The inset shows the size dependence of the thermal hysteresis loop width. The parameters' values used in the simulations are $J/k_B=45K$, $G/k_B=105K$, $\Delta/k_B=1300K$, $\ln(g)=6$.

Figure 3.12 shows a series of simulated thermal hysteresis loops obtained on a cubic system when its size is decreased from $N=60 \times 60 \times 60$ molecules to $N=4 \times 4 \times 4$ molecules. N represents the number of bulk SCO molecules (active molecules) and the edge molecules, on each face of the cubic system trapped in the HS state. Then the total number of molecules in the system is: $M = (60+2) \times (60+2) \times (60+2)$ molecules.

In figure 3.13 is reported the shape effect for a 2D system considering the edge molecules as active molecules that interact with their local environment. As we can see in figure 3.13 the behavior is strongly influenced by the edge effect. By decreasing the system's cooperativity the transition is shifted to lower temperatures and occurs with hysteresis contrary to the cases when the edge molecules are fixed in HS state.

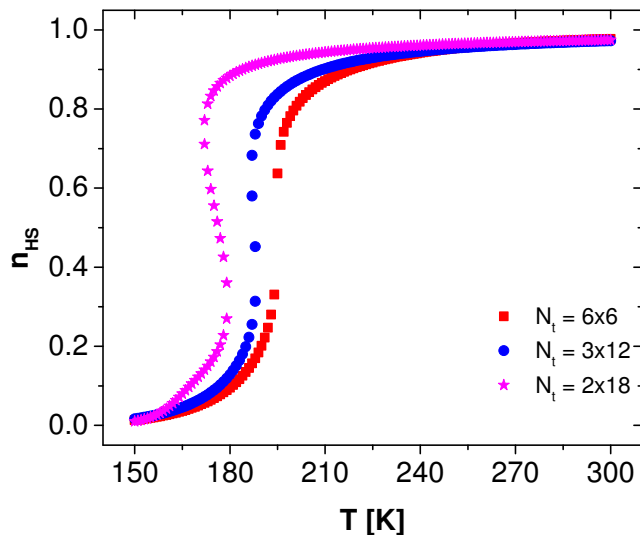


Figure 3.13 The thermal behaviour for different shapes of a 2D system containing 36 molecules. The computational parameters are: $\Delta/k_B = 1300$ K, $J/k_B = 15$ K, $G/k_B = 172.7$ K, $L/k_B = 120$ K, $\ln(g) = 6.01$, $N = 36$.

4 Analysis of spin crossover nanochains using parabolic approximation in the framework of Atom-phonon coupling model

4.1 Introduction

Considering atoms that are linked by springs characterized by three elastic constants as a function of the atom's state, Nasser et al. propose [93,121] the APC model to give a clear and enlarged view of the ST process in the SCO compounds. Although the APC model has only been applied to 1D and 2D systems thus far, different behaviors under various external stimuli, such as: temperature [121-123], pressure [124], light [125,126] have already been reported using APC.

In this chapter the atom-phonon coupling model is used to explain and illustrate the behavior of a linear chain of molecules pertaining to SCO compounds. It is well known that apart from the system's cooperativity, which influences the hysteretic behavior of SCO complexes, the size of the system also plays a determinant role. The properties of the system are analyzed using a parabolic algorithm as a new method proposed in order to take into account the phonon contribution. Based on exact calculations, this method is closer to reality and more efficient than the mean-field approximation (MFA). In particular, both the parabolic algorithm and the dynamic-matrix method are tested and compared and the analysis of the system's behavior shows that large size systems can be treated without generating all the system states. We also analyzed the role of degeneracy, and the thermal variation of both the entropy and heat capacity in the ferromagnetic-like coupling case. These studies play an important role in the choice process of SCO compounds for the desired application. Thus, it is known that the compounds that exhibit transition with hysteresis have the main domain of application the memory devices. The compounds with a gradual transition, with a weak cooperativity, are destined to sensors devices. So, before to build a sensor it is important to know how to choose the compound according to the cooperativity and how will be influenced the behavior by interaction with other perturbation factors.

The originality of the APC model comes from the assumption that the neighboring molecules are connected by a spring whose elastic constant depends on the molecular states. Because the intra-molecular vibrations are not taken into account in the model, the SCO molecules are treated as atoms. Thus, the three elastic constants are defined as: $\lambda=C_{LL}$ when both the atoms are in the LS state, $\mu=C_{LH}$ when one atom is in a LS state and the other atom in a HS state, and $\nu=C_{HH}$ when both the atoms are in a HS state (figure 4.1). This makes the Hamiltonian of the system easy to cast.

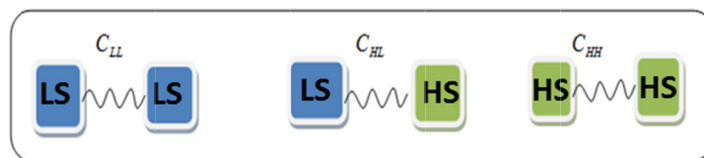


Figure 4.1 Schematic representation of the elastic constants related to the three molecular configurations.

The APC Hamiltonian solved with the dynamic matrix method gives the exact solution for the system. Within MFA, which has been used to solve the Hamiltonian for 1D and 2D systems, we illustrate, for the first time in this paper, how the corresponding Hamiltonian can be solved using the parabolic method. Recall that it is known that the MFA gives different

results to those of the dynamic matrix method because the MFA replaces the three elastic constants with only one constant.

In this work we use the parabolic method to solve the Hamiltonian model considering three representative configurations: the “ferromagnetic” LS-LS and HS-HS and the antiferromagnetic LS-HS. We first study the differences between the dynamic-matrix method, the MFA, and this new approximation (the parabolic method). A second part of our work is devoted to the influence of the degeneracy in the parabolic method. Lastly, we study the entropy and the heat capacity starting from a small size (number of molecules $N=8, 20$) to a larger one ($N=100$ molecules) for different elastic interaction strengths between the molecules.

4.2 The model

To study the behavior of SCO systems in the framework of the APC model, we considered a circular chain of N atoms interconnected by a spring, with elastic constants as already described in the introduction; where $\lambda > \mu > \nu$. To present the electronic state of the atoms, we associate to each electronic state of the atoms a fictitious spin operator σ which has two eigenvalues $+1$ or -1 as a function of the atom state (HS or LS respectively).

The total Hamiltonian of the chain can be written as the sum of spin and phonon contributions as:

$$H = H_{spin} + H_{phonon} \quad (4.1)$$

From the definition of Δ which is the difference in energy between the two electronic levels (LS) and (HS), the spin Hamiltonian and phonon Hamiltonian can be expressed as:

$$H_{spin} = \sum \frac{\Delta}{2} \sigma_i \quad (4.2)$$

$$H_{phonon} = \sum g^{nhs} B(f_i) \quad (4.3)$$

where $B(f_i)$ is the Boltzmann factor for each configuration(i).

4.3 Results and discussions

For a number N of atoms we can generate all the possible configurations as sketched in figure 4.2. In this case we explore all the possibilities which are in good agreement with a real system.

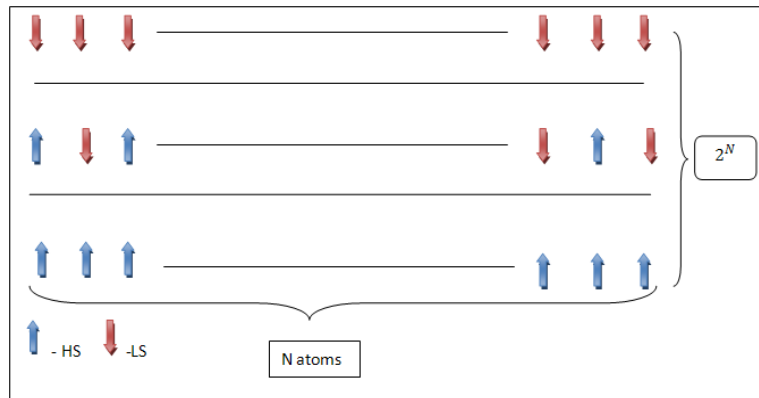


Figure 4.2 Schematic representation of the possible atoms' configurations in the chain.

Solving the system's Hamiltonian (equation (3.2)) by using either of the above three mentioned methods, allows the determination of the HS fraction n_{HS} as function of temperature.

Figure 4.3a and figure 4.3b show numerical results concerning the evolution of HS fraction. Before presenting in details the next figure, we recall that the Ising like models lead to phase transitions when the balance between short-range and long-range interactions allow cooperative effects.

In the APC model the x and y reduced parameters are introduced as follows:

$$x = \frac{\nu}{\lambda} \quad (4.4)$$

$$\mu = \frac{\lambda + \nu}{2} + \frac{\lambda - \nu}{2} y \quad (4.5)$$

The parameter y is related to the short-range interaction: $y=0$ corresponds to the absence of short range interaction. $y>0$ and $y<0$ are related to the "ferromagnetic-like" and "anti-ferromagnetic-like" coupling respectively.

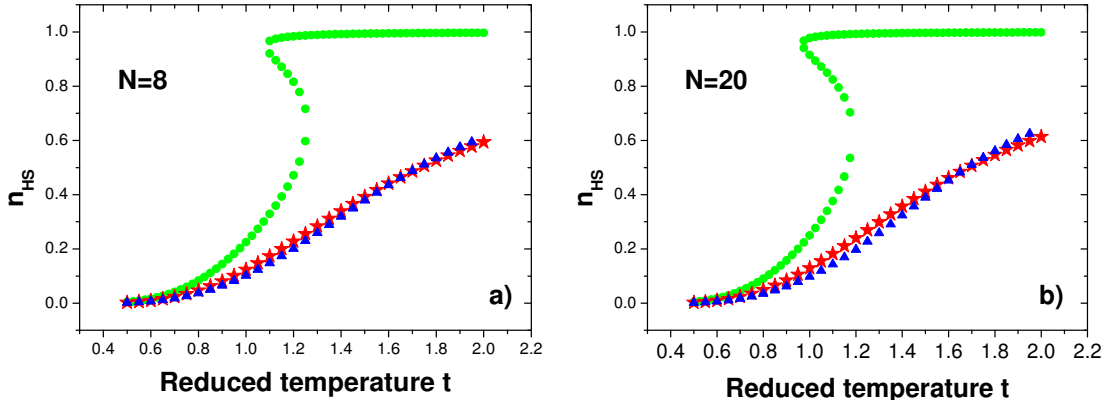


Figure 4.3. The thermal variation of high spin fraction n_{HS} for a 1D SCO compound a) $N=8$ molecules b) $N=20$ molecules using the MFA method (circles), the Parabolic method (triangles), the Dynamic matrix (stars). Other parameter are $x=0.2$, $y=0.2$, $g=5$ and $\delta=4$.

Figures 4.3a and 4.3b display the evolution of HS fraction given by the three methods for a chain of $N=8$ molecules (figure 4.3a) or $N=20$ molecules (figure 4.3b) with the calculated values plotted as circles, triangles and stars. The circles correspond to the date obtained within the MFA method; the triangles within the parabolic method and the stars within the dynamic matrix method.

For regular interactions strength corresponding to $x=0.2$ and $y=0.2$, the variation displayed in figures 4.3a and 4.3b shows that the parabolic method gives the same results as the dynamic matrix method, that is a gradual transition. In the frame-work of the MFA method, the system displays a hysteretic behaviour with a hysteresis width equal to 0.15 for $N=8$ molecules and 0.2 for $N=20$ molecules. Furthermore, the critical temperature $T_{1/2}$, which corresponds to $n_{HS}=0.5$, is shifted to higher temperatures when the system's size is increased. Here it is worth noting that the MFA method gives a hysteretic behavior because it generates artificially infinite long-range interactions.

4.3.1 Role of parameters in the parabolic algorithm

In this section the main goal is to develop a method to study large systems (high number of molecules) through the parabolic algorithm without having to generate all the state

distribution as with the dynamic matrix method. To validate our new method we first study in this section the key factors which influence the curves calculated with the parabolic algorithm by considering only short range interactions on the one hand and then both short and long range interactions on the other.

The thermal dependence of the HS fraction obtained using both methods: the dynamic matrix and the parabolic method, for various values of the degeneracy is reported in figure 4.4. The presence of short-range interactions has an important contribution on the system's behavior and leads to a gradual spin conversion. The results obtained within both methods are in excellent agreement as shown in figures 4.4.

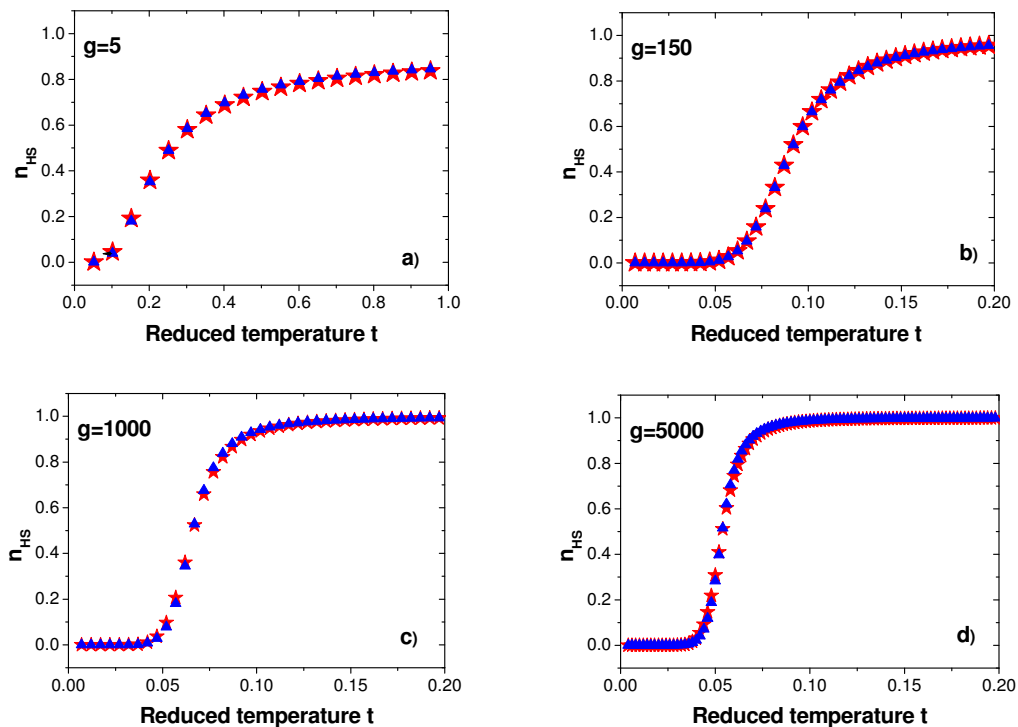
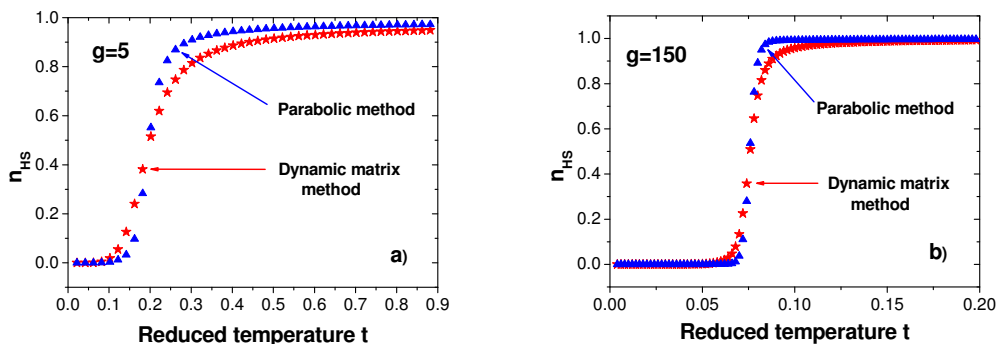


Figure 4.4. The thermal variation of the high spin fraction n_{HS} for a 1D SCO compound ($N=8$ molecules) for different degeneracies a) $g=5$ b) $g=150$ c) $g=1000$ d) $g=5000$ using, the Parabolic method (triangles), the Dynamic matrix (stars). Other parameter are $x=0.3$, $y=0$, and $\delta=0.6$.

The system's behavior when both the short-range interactions and long-range interactions are taken into account is shown in figure 4.5 in the limiting case, when the system presents strong interactions ($x=0.1$, $y=0.9$).



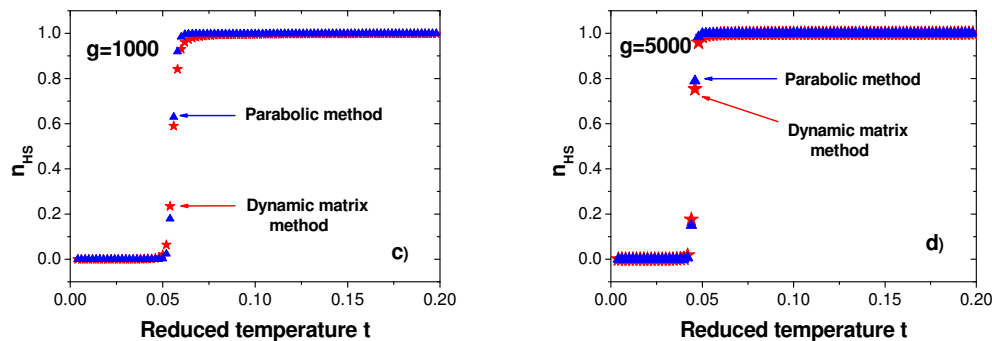


Figure 4.5. The thermal variation of n_{HS} for a 1D SCO compound ($N=8$ molecules) for different degeneracy values a) $g=5$ b) $g=150$ c) $g=1000$ d) $g=5000$ using the Parabolic method (triangle curve), the Dynamic matrix (stars curve). The following computational parameters have been used: $x=0.1$, $y=0.9$, and $\delta=0.6$.

4.3.2 Entropy variation and heat capacity using the dynamic matrix method vs. the parabolic method

Following the results given in the previous section showing the good agreement between the exact method (dynamic matrix) and the parabolic method, at high degeneracies, the thermal dependence of the entropy and heat capacity for different interactions and sizes were calculated under these conditions. The system entropy could be calculated as the first derivative of the Gibbs free energy with respect with the temperature $S = -dF/dt$.

Both the parabolic method and the dynamic matrix method lead to the same curves and the same evolution between the LS and HS states as shown in figures 4.6.

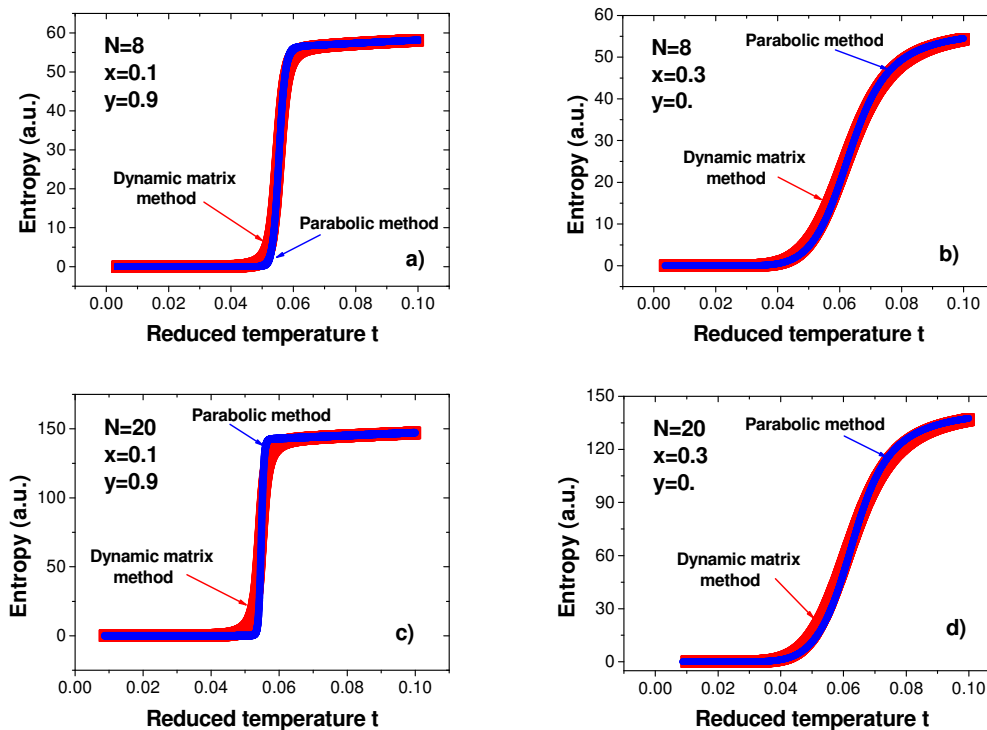


Figure 4.6. Time dependence of the entropy per atom obtained using: the dynamic matrix method (red curve) and the parabolic method (blue curve) for two different sizes and interactions. Other parameter are $g=1000$ and $\delta=0.6$.

Figure 4.7 display the evolution of the heat capacity as calculated from the relationship, $C = dS/dt$ for a chain which contains 8 molecules (figures 4.7a and 4.7b) and 20 molecules (figures 4.7c and 4.7d). The two methods, this time show a difference in the evolution of heat capacity in all cases. The heat capacity curves obtained with the exact method have a lower maximum compared with those obtained using the parabolic method because the total free energy of the system for a given temperature obtained using the exact method is less than the total free energy of the system given by the parabolic method.

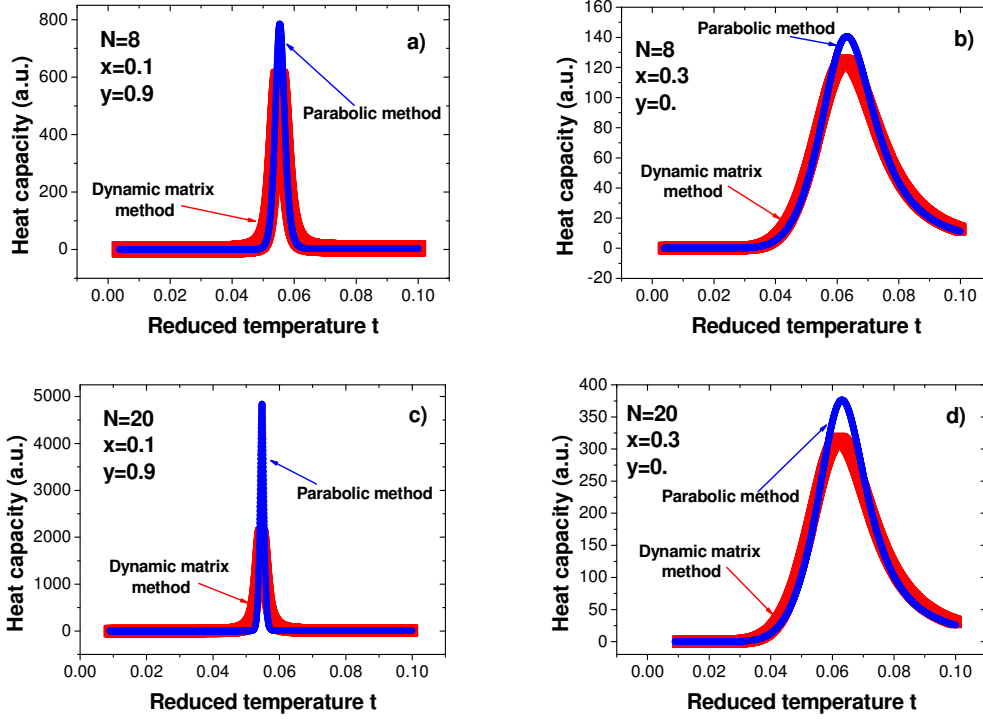


Figure 4.7. Time dependence of the heat capacity obtained using: the dynamic matrix method (red curve) and the parabolic method (blue curve) for two different sizes and interactions. Other parameter are $g=1000$ and $\delta=0.6$.

The dynamic matrix method needs a higher computation power than the parabolic one, because it is necessary to generate all the 2^N (N = number of molecules) states of the system. For large systems, the parabolic method becomes more attractive and easier to apply from this point of view.

4.4 The role of edge atoms using the dynamic matrix transfer and the free energy methods

Using Monte Carlo Metropolis (MCM) algorithm described in [127] the switching probability between the old state and the new state, P , is given by the following equation:

$$P_{state} = \frac{g^{nhs_{new}} e^{-\frac{\beta\Delta}{2}m_{new}} \prod_{i=1,N} \left[2\sinh\left(\frac{\hbar\omega_{new}}{2k_B T}\right) \right]^{-1}}{g^{nhs_{old}} e^{-\frac{\beta\Delta}{2}m_{old}} \prod_{i=1,N} \left[2\sinh\left(\frac{\hbar\omega_{old}}{2k_B T}\right) \right]^{-1}} \quad (4.6)$$

In the free energy method the magnetization M is calculated as follows:

$$M = \frac{\sum m_i \deg \xi_i}{\sum \deg \xi_i} \frac{1}{N} \quad (4.7)$$

where \deg is the number of configurations with the same eigen value.

The high spin fraction n_{HS} giving the ratio between the number of atoms in the high spin state and the total number of atoms is defined as:

$$n_{HS} = (1 + M) / 2 \quad (4.8)$$

Using the following formula to calculate the free energy, F , we are able to study the stability of the system's state:

$$F(n_{HS}) = -T \ln \left(\sum_{i=1}^N \xi_i \right) \quad (4.9)$$

To explain the role of edge atoms two types of systems were considered: an **A** type system in which the molecules are either HS and (or) LS and a **B** type system in which we add and fix at the beginning and at the end, one atom in the HS state to an **A** type system. In this case the system **A** can be **HS.....HS-LS.....LS** while the system **B** is of the form **HS+LS.....HS-LS.....LS+HS**. Figure 4.8 a) and b) show the evolution of the HS fraction, n_{HS} , as a function of temperature and the free energy for three different temperatures. In figure 4.8 a) besides the red curve, when the temperature is increasing and the blue curve when the temperature is decreasing (obtained by the transfer matrix method and the MCM algorithm), the results obtained by the numerical calculation previously described are plotted in black.

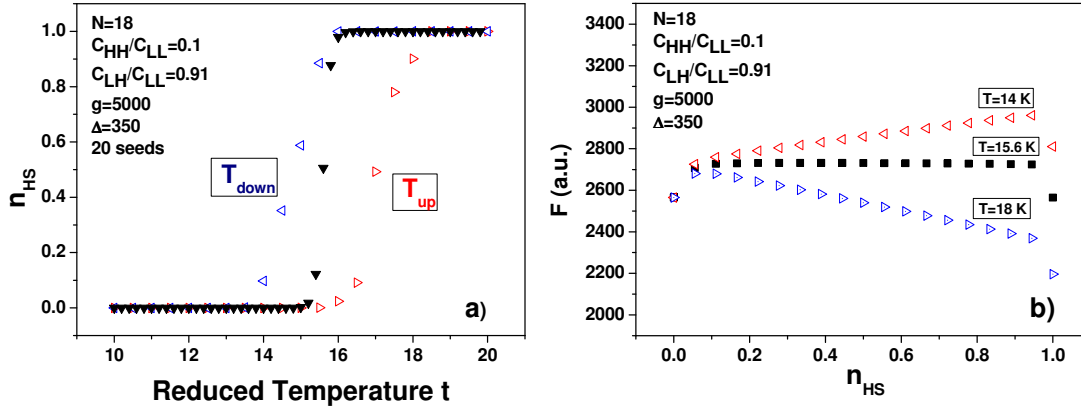


Figure 4.8. a) the simulated HS fraction, n_{HS} , as a function of the temperature and b) the free energy for three different temperatures for an **A** type system.

In figures 4.9 a) and b) are reported the HS fraction and the free energy for three different temperatures for a **B** type system. The comparison of the results reported in figure 4.9 a) with figure 4.9 a) shows that by adding and fixing the edge atoms in the HS state, the transition temperature is shifted to a lower temperature and the width of the hysteresis loop is decreased. Moreover the transition is more abrupt.

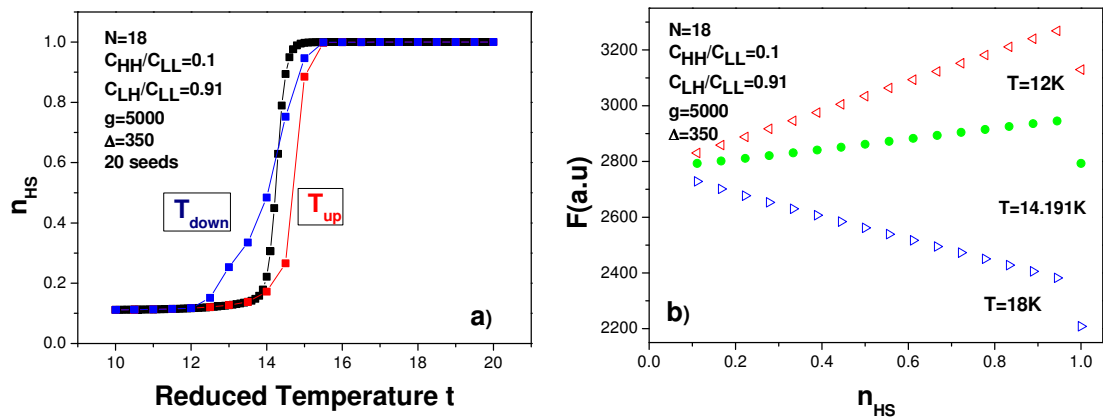


Figure 4.9 a) the simulated HS fraction, n_{HS} , as a function of the temperature and b) the free energy for three different temperatures for a **B** type system.

5 Pressure effect in molecular spin crossover compounds

5.1 Analysis of the P-T- n_{HS} phase diagram of $[\text{Fe}(\text{hyptrz})]_2\text{A}_2\cdot\text{H}_2\text{O}$ spin crossover 1D coordination polymer

One remarkable successful model used in the description of bistable SCO systems is the Ising-like model, which describes interacting two-level units; the energy levels having different energies and degeneracies [19]. In this chapter, the Ising-like model was used for describing both static and dynamic properties of SCO compounds under different external stimuli such as temperature and pressure [128,129].

Described in the chapter 1, in this chapter are recalls only some important equations of Ising like model. So, the Ising Hamiltonian can be written as follows:

$$H = \frac{\Delta - k_B T \ln g}{2} \sum_i \hat{\sigma}_i - J_{i,j} \sum_{\langle i,j \rangle} \hat{\sigma}_i \hat{\sigma}_j - G \sum_{\langle i \rangle} \hat{\sigma}_i \langle \hat{\sigma} \rangle \quad (5.1)$$

where $\hat{\sigma}$ is the fictitious spin operator with the eigen values +1 (when the molecule is in the HS state) and -1 (when the molecule is in the LS state); $\sum_{\langle i,j \rangle}$ - denotes the sum over nearest neighbouring spins; the gap energy, $\Delta = E(\text{HS}) - E(\text{LS})$ is the internal energies differences between the HS and LS; the term $k_B T \ln g$ take into account the entropy contribution (g is the degeneracy ratio); $J_{i,j}$ stands for the short-range interaction parameter that represents the cooperative interaction that only exists between the nearest neighboring pairs ($J_{i,j}$ includes the nearest neighbors number) and finally G is long range interaction parameter. The equilibrium temperature $T_{1/2}$ for which $n_{HS} = n_{LS} = 1/2$ corresponds to a zero effective field, irrespectively of the interactions: $T_{1/2} = \Delta/k_B \ln g$.

5.1.1 Pressure effect

Over the last few years an important effort has been done by different laboratories to explain, experimentally [71,105,130-136] or theoretically [90,124,137-139], different unusual behaviors of SCO complexes under an external applied pressure. Due to the change in the metal-ligand bond length when the SCO occurs, these materials are highly sensitive to an external applied pressure. The bistable properties at the molecular level are adequately described through a molecular configurational diagram, i.e. a plot of the adiabatic energy vs. the distortion coordinate of the molecular system. Indeed, it is already known that by applying an external pressure the energy gap is increasing, due to the decrease of the metal-ligand bond length, and by consequence the activation energy, E_a will decrease and the LS state will be stabilized.

The pressure dependence of the energy gap is:

$$\Delta(T, p) = \Delta(T, p = 0) + p \delta V \quad (5.2)$$

where δV is the volume variation and p is the external applied pressure.

Assuming that all sites are equivalent, the mean field treatment is performed as usual, so that the one-site mean field Hamiltonian can be written as:

$$H_{equiv} = \frac{\Delta(T, p)}{2} \hat{\sigma} - (qJ + G) \hat{\sigma} \langle \hat{\sigma} \rangle \quad (5.3)$$

where q is the nearest neighbors number, $\langle \hat{\sigma} \rangle = m$ is the „fictitious magnetization”, that can be written as:

$$\langle \hat{\sigma} \rangle = m = \tanh \left(\frac{(qJ + G)m}{k_B T} + \frac{k_B T \ln g - \Delta(T, p)}{2k_B T} \right) \quad (5.4)$$

For the sake of simplicity, in calculations we used the following reduced parameters: the reduced energy gap, $\Delta = \Delta(T, p) / k_B$, reduced interaction parameter $\Gamma = (qJ + G) / k_B$, (which contains the short and long range contribution) and reduced volume variation, $\alpha = \frac{\delta V}{k_B} 10^{-5}$ (the factor 10^{-5} stands for the pressure units conversion from Pascal to Bar).

The HS fraction is usually expressed as a function of a fictitious magnetization m : $n_{HS} = (m + 1) / 2$.

Equation (5.4) allows to plot both thermal and pressure dependence of the HS fraction, as shown in figure 5.1.

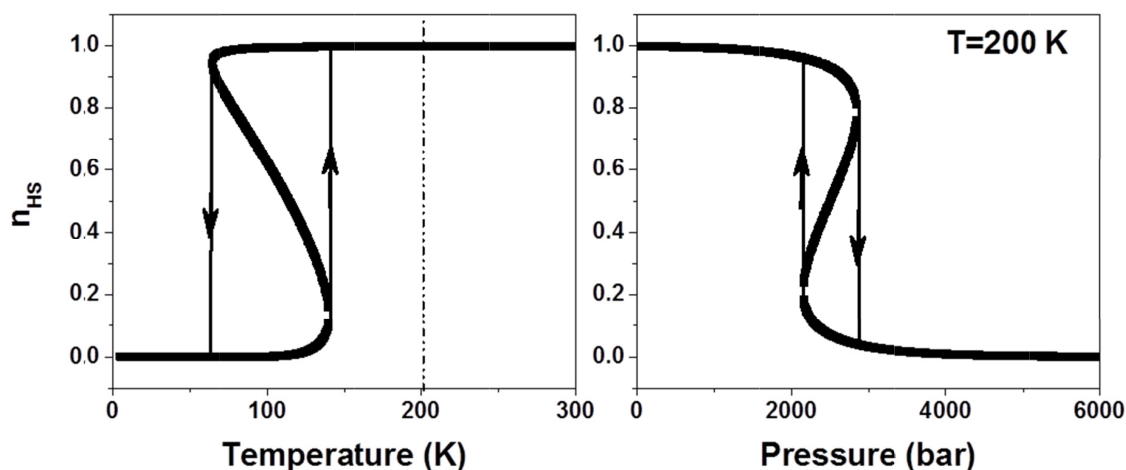


Figure 5.1 Simulated thermal hysteresis loop, at ambient pressure (a) and pressure hysteresis loop, recorded at 200 K (b). The values of the parameters used in calculations are: $\Delta/k_B=800\text{K}$, $\Gamma/k_B=300\text{K}$, $\ln(g)=7$ and $\delta V=13.2 \text{ \AA}^3$.

In order to use SCO molecular systems in temperature and pressure sensing devices the system’s output signal (HS fraction in our case) should be linearly dependent on the input perturbation, i.e. temperature and/or pressure variation in our case [25]. Thus, the best characteristics will be demonstrated by a very low cooperative SCO system, which exhibits a gradual spin conversion as linear as possible.

5.1.2 Pressure-Temperature (p-T) phase diagram

The color change associated to the spin state switching of some SCO complexes makes possible to track the HS molar fraction evolution under the influence of different stimuli by optical methods. We used a gas pressure cell equipped with a safire optical window and a cryostat. The experimental setup has been described elsewhere [134,140], as well as the synthesis of the thermochromic 1D SCO coordination polymer $[\text{Fe}(\text{hyptrz})]\text{A}_2 \cdot \text{H}_2\text{O}$ (hyptrz=4-(3’-hydroxypropyl)-1,2,4-triazole and A = 4-chloro-benzenesulfonate) [141].

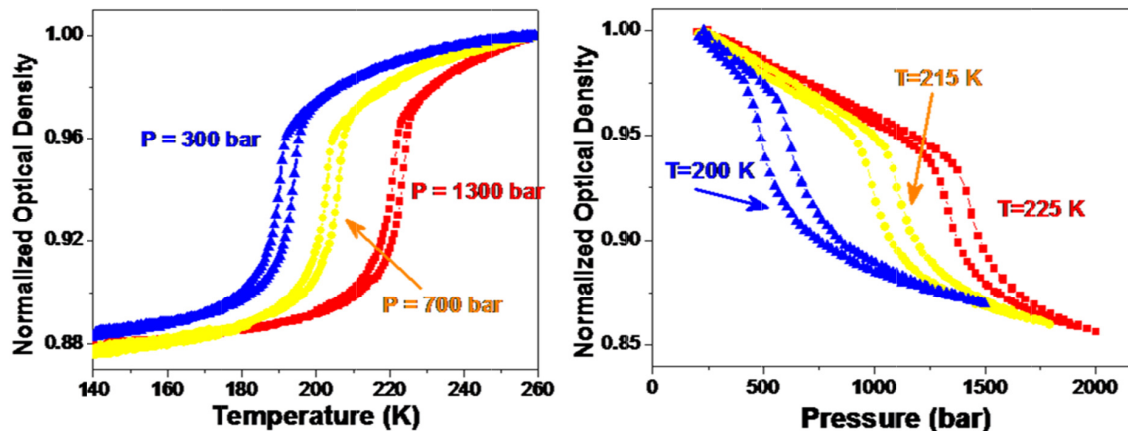


Figure 5.2 Selected thermal (left) and pressure (right) hysteresis loops recorded at several pressures and temperatures, respectively for $[\text{Fe}(\text{hyprtz})]_2\text{A}_2\cdot\text{H}_2\text{O}$.

Several thermal hysteresis loops under different pressures and pressure hysteresis loops taken at different temperatures have been successfully recorded for $[\text{Fe}(\text{hyprtz})]_2\text{A}_2\cdot\text{H}_2\text{O}$ (Figures 5.2 and 5.3). Figure 5.2 illustrates the thermo- and piezochromic behavior of the 1D polymer under an external applied pressure. When the pressure is increased, the transition temperatures shift higher with 33 K/kbar and the hysteresis width decreases progressively (figure 5.3). A similar effect is observed for the pressure hysteresis loop where the hysteresis width is decreasing with the increase of temperature (figure 5.2). These results allow us to plot the experimental 2D (p-T) phase diagram (figure 5.3).

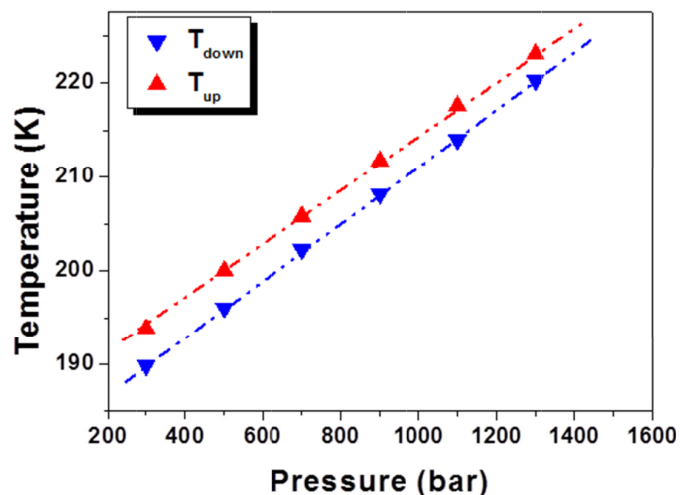


Figure 5.3 Experimental 2D p-T phase diagram recorded on $[\text{Fe}(\text{hyprtz})]_2\text{A}_2\cdot\text{H}_2\text{O}$.

Figure 5.4 displays the experimental 3D (p-T- n_{HS}) phase diagram recorded by diffuse reflectivity, which is only partial because of the limitation of our experimental setup (the maximum reached pressure was ~ 2 kbar). However our setup allowed us to change the pressure in small steps of about 10 bars in both loading (increasing pressure) and unloading (decreasing) modes. We should mention herein that the pressure effect on this SCO complex has been already studied elsewhere by using a clamp type pressure cells [141,142]. In this study a reentrance phenomenon under pressure of $[\text{Fe}(\text{hyprtz})]_2\text{A}_2\cdot\text{H}_2\text{O}$ was revealed. However, in this work the authors resumed their study to record the thermal behavior at different external pressures. This unusual effect has been explained in the frame-work of the atom-phonon coupling model by considering that the elastic constant value of an

antiferromagnetic configuration (HS-LS) is closer to the value of the elastic constant of a HS-HS configuration [137].

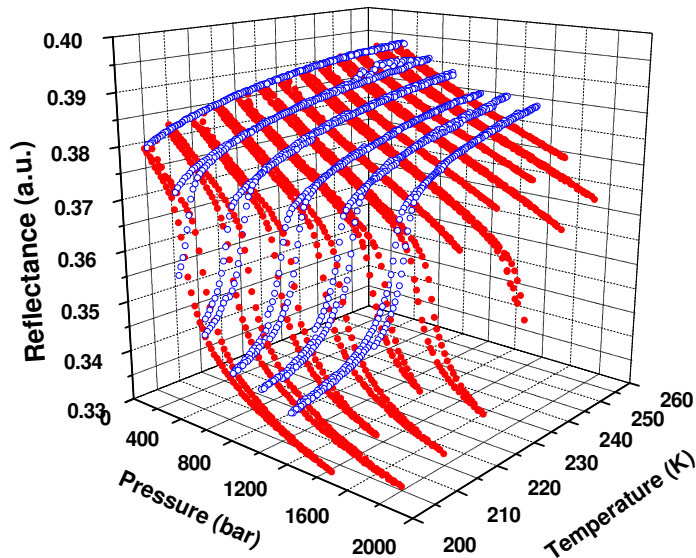


Figure 5.4 Incomplete experimental 3D (p-T- n_{HS}) phase diagram recorded on $[\text{Fe}(\text{hyptrz})]\text{A}_2\cdot\text{H}_2\text{O}$.

5.2 Impact detection using SCO materials

The continuous developments of chemical systems allows the selection of the best SCO systems with special requirements concerning the SCO temperature region, which need to be located around room temperature region as well as the width of their bistability domain which need to be as large as possible. Following these conditions, we decided to focus on the 1D chain $[\text{Fe}(\text{hyetrz})_3]\text{I}_2\cdot\text{H}_2\text{O}$ (hyetrz = 4-(2'-hydroxyethyl)-1,2,4-triazole) as a suitable candidate. This material is known to exhibit a cooperative and thermo chromic spin transition from LS ($S = 0$, violet) to HS ($S = 2$, white) around the room temperature region [143]. In this work we show that $[\text{Fe}(\text{hyetrz})_3]\text{I}_2\cdot\text{H}_2\text{O}$ can be used as a visual detector of strong mechanical contact pressure from 25 MPa to 250 MPa. This result is supported by thermal dependence of the optical reflectivity measurements, ^{57}Fe Mössbauer spectroscopy and differential scanning calorimetry. A correlation of SCO properties with the pressure contact is made thanks to an Ising-like model. These results provide the basis for the construction of a marker pressure device.

5.2.1 Results and discussions

The colour change of the sample from white (HS) to violet (LS) was monitored through variable-temperature optical reflectivity measurements in a dry nitrogen atmosphere at 2 K/min. The thermal dependence of the diffuse reflectance has been recorded, simultaneously, spectroscopically and at a quasi-monochromatic wavelength of $\lambda = 550(50)$ nm (see figure 5.5).

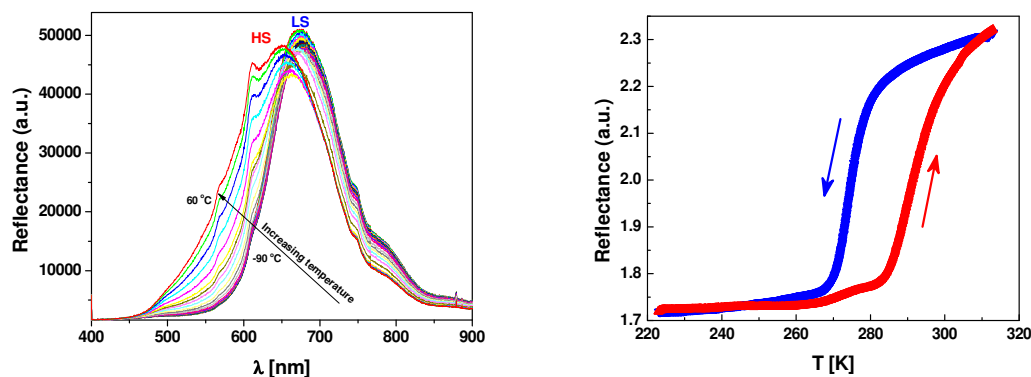


Figure 5.5 Thermal evolution of reflectance spectra recorded on $[\text{Fe}(\text{hyetrz})_3]\text{I}_2 \cdot \text{H}_2\text{O}$ in the solid state (left) and of the optical density at $\lambda = 550$ nm (right).

The hysteretic SCO behaviour around room temperature is confirmed for $[\text{Fe}(\text{hyetrz})_3]\text{I}_2 \cdot \text{H}_2\text{O}$ at $T_c^\uparrow = 292$ K and $T_c^\downarrow = 275$ K by optical reflectivity measurements (figure 5.5). The high colour contrast of the sample, between the two spin states, can be tracked by recording temperature dependence of the reflectance spectra. The optical characterization has been completed by differential scanning calorimetric (DSC) measurements which were undertaken to confirm the spin transition temperature range as well as to determine, quantitatively, the thermodynamic parameters to be used in our Ising model described hereafter.

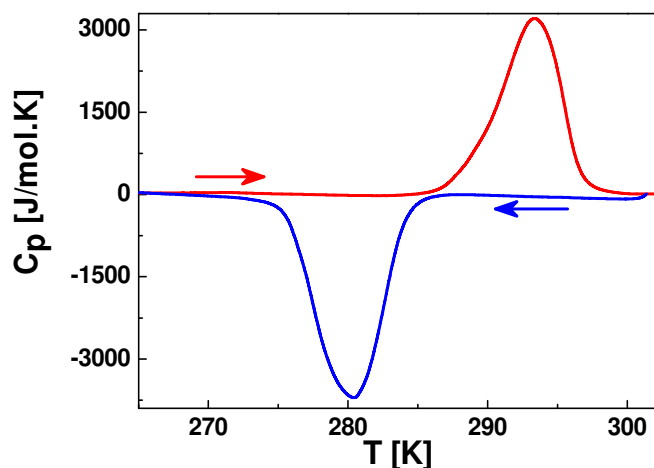


Figure 5.6 DSC curves for $[\text{Fe}(\text{hyetrz})_3]\text{I}_2 \cdot \text{H}_2\text{O}$ over the 265-303 K temperature range.

The DSC curve, recorded at 10 K/min in the heating and cooling modes (figure 5.6), shows an endothermic peak at $T_{max}^\uparrow = 293$ K and an exothermic peak at $T_{max}^\downarrow = 280$ K, in fair agreement with the transition temperatures observed from optical measurements. The difference seen in the lower branch of the spin transition curve is associated to the lower scan rate (2K/min) used for the optical measurements.

Pressure experiments were carried out on a home-made micromechanical device. The sample was deposited on a metal plate and covered with a scotch tape (figure 5.7).

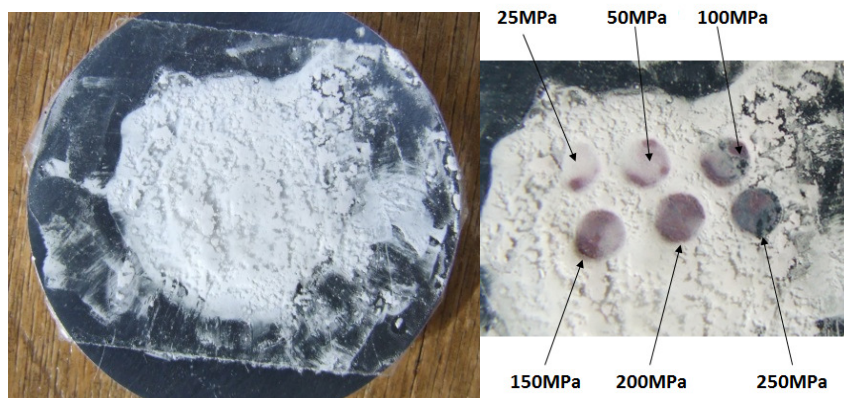


Figure 5.7 (Left): sample holder showing the SCO compound at room temperature on its sample holder covered with a scotch tape. (Right): Enlarged view of the sample evidencing colour change to pink at room temperature for various applied pressures (25 MPa, 50 MPa, 100 MPa, 150 MPa, 200 MPa and 250 MPa).

As shown in figure 5.7, the material is white at room temperature and ambient pressure which is characteristic of the HS state. The pressure was applied at selected spots on the sample, released and a photograph was taken again. As it can be seen, for a threshold value of the applied pressure of ca. 30 MPa, the SCO powder switches from white (HS) to pink (LS) and retain its colour (spin state) when pressure is released. On warming to 303 K, the powder switches back to white (HS state), making the sensor reusable.

The thermal and pressure dependence of the HS molar fraction, n_{HS} , at ambient pressure and temperature, computed for $[\text{Fe}(\text{hyetrz})_3]\text{I}_2 \cdot \text{H}_2\text{O}$, i.e. for a complex displaying a hysteretic spin transition around room temperature is displayed in figure 5.8. The transition temperatures at atmospheric pressure are $T_c^\uparrow = 292.5$ K and $T_c^\downarrow = 278.8$ K, which are in excellent agreement with the ones detected by optical reflectivity (figure 5.9). The transition pressures at 300 K are $P_c^\downarrow = 17.5$ MPa and $P_c^\uparrow = 8.2$ MPa.

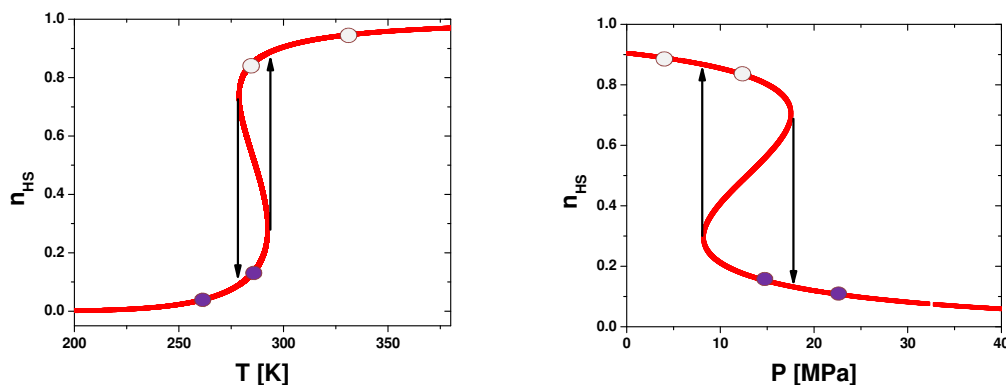


Figure 5.8 Thermal dependence at 1 bar (left) and pressure dependence at 300 K (right) of the HS molar fraction, n_{HS} , as derived from the Ising like model. The parameters values are $\Delta_0/k_B = 1978.6$ K, $\delta V = 100$ A³, $\ln(g) = 6.906$ and $\Gamma/k_B = 360$ K.

A (P-T) phase diagram was generated to better understand the influence of temperature and pressure on the SCO behaviour. The calculated phase diagram in pressure-temperature coordinates using the same parameters as in figure 5.8, is displayed in figure 5.9.

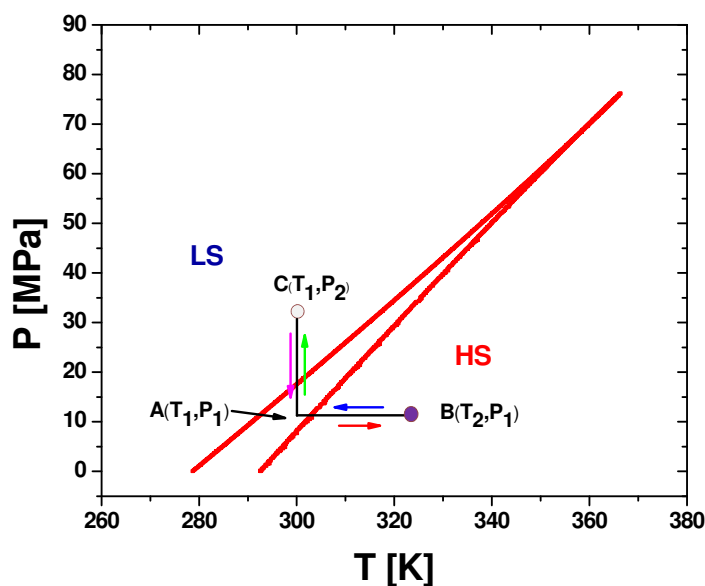


Figure 5.9 Pressure-temperature phase diagram calculated for a SCO system switching around the room temperature region using the following parameters values: $\Delta_0/k_B = 1978.6$ K, $\delta V = 100$ A³, $\ln(g) = 6.906$ and $\Gamma/k_B = 360$ K.

As can be seen from figure 5.9, the transition from the HS to the LS state can be achieved either by decreasing the temperature or by increasing the pressure. When the SCO compound located at point **A**, i.e. at given temperature T_1 and pressure P_1 , is heated until it reaches point **B** of temperature $T_2 \geq T_{up}$ at a constant pressure P_1 , a switch back to the HS state is observed. From **B**, if the temperature is decreased until it gets back to point **A** (T_1, P_1) then the compound remains in the HS state. By applying a pressure, the compound switches from HS to LS states at point **C** ($T_1, P_2 > P_{down}$). If now the pressure is lowered back to P_1 (point **A**), the compound will remain in the LS state. In other words, inside the hysteresis width, the compound will keep the state of origin. When coming from the LS state it will remain in the LS state and when coming from the HS state it will retain the HS state as shown in figure 5.10.

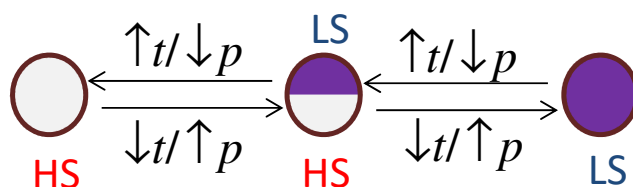


Figure 5.10 Representation of the switching mechanism induced by temperature and/or by pressure.

5.3 Sensor concept

The use of SCO compounds as active components in thermal and pressure sensor devices was discussed in a few papers [25,27,144], but did not yet considered the attractive possibility to monitor at the same time both pressure and temperature due to the existence of multiple sets of T, P solutions that results from the p - T phase diagram. In this subsection is presented a novel concept for spin crossover-based sensors that allow the concomitant detection of both temperature and pressure using two different SCO materials that exhibit

gradual transitions. So, let's consider two SCO materials characterized by the following parameters:

- compound 1: Δ_1 , δV , g_1 and Γ_1 ;
- and compound 2: Δ_2 , δV , g_2 and Γ_2 .

The fictitious magnetizations, according with equation (5.4), of the two compounds can be written as:

$$\begin{cases} \langle \sigma_1 \rangle = \tanh \left(-\frac{\Delta_1 + pc\delta V - T \ln g_1 - 2\Gamma_1 \langle \sigma_1 \rangle}{2T} \right) \\ \langle \sigma_2 \rangle = \tanh \left(-\frac{\Delta_2 + pc\delta V - T \ln g_2 - 2\Gamma_2 \langle \sigma_2 \rangle}{2T} \right) \end{cases} \quad (5.5)$$

where c is a constant equal to 0.0724, when the external applied pressure, p , is expressed in MPa and the volume variation of the molecule, δV , is expressed in \AA^3 .

Now, by solving the system of Equations (5.5), the expressions for T and p can be written as:

$$\begin{cases} T = \frac{2\Gamma_1 \langle \sigma_1 \rangle - \Delta_1 - 2\Gamma_2 \langle \sigma_2 \rangle + \Delta_2}{2 \tanh^{-1} \langle \sigma_1 \rangle - \ln g_1 - 2 \tanh^{-1} \langle \sigma_2 \rangle + \ln g_2} \\ p = \frac{(2\Gamma_1 \langle \sigma_1 \rangle - \Delta_1) * (2 \tanh^{-1} \langle \sigma_1 \rangle - \ln g_1 - 2 \tanh^{-1} \langle \sigma_2 \rangle + \ln g_2) - (2\Gamma_2 \langle \sigma_2 \rangle - \Delta_2) * (2 \tanh^{-1} \langle \sigma_1 \rangle - \ln g_1)}{c\delta V * (2 \tanh^{-1} \langle \sigma_1 \rangle - \ln g_1 - 2 \tanh^{-1} \langle \sigma_2 \rangle + \ln g_2)} \end{cases} \quad (5.6)$$

From the system of Equations (5.6) we can find simultaneously both values of temperature and pressure knowing the values of $\langle \sigma_1 \rangle$ and $\langle \sigma_2 \rangle$. These values can be obtained by identifying the optical densities of each complex. The projected device must be initially calibrated using their optical densities. Compounds that could be adapted to this device should exhibit gradual transitions. Practically, our concept can be described as follows. A monochromatic light source (green light = 540 nm) is sent to both compounds. The "scattered" or reflected light by the compounds are directed on the detector (see Figure 5.11). The detector, calibrated previously, will assign the $\langle \sigma_1 \rangle$ and $\langle \sigma_2 \rangle$ that corresponds to the lights coming from both compounds. The temperature and pressure values are obtained by replacing the $\langle \sigma_1 \rangle$ and $\langle \sigma_2 \rangle$ in Equations (5.6). The challenge for chemists will be to synthesize SCO compounds with a good optical contrast and which will be thermally, pressure and time stable. In other words, to elaborate samples which keep the same color over time at a defined temperature and pressure set. This objective looks not too far to be achieved considering recent developments in the SCO field.

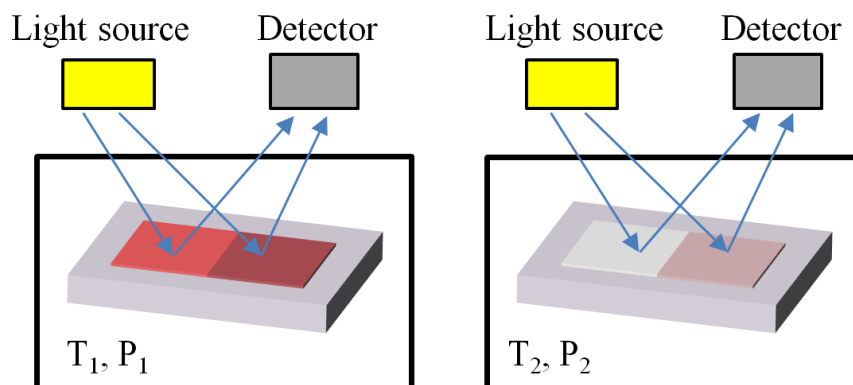


Figure 5.11 Principle of measuring simultaneously temperature and pressure using two SCO compounds with optical reflectivity detection.

General Conclusions

The continuous development of new equipment and machinery that require more advanced sensors with improved technical characteristics constitutes the motivation behind the results presented in this thesis. A special class of new sensors is based on spin-crossover materials. The main advantages of these materials, such as the ability to be controlled at the molecular level, color changing during the transition between the two states, hysteresis, and high sensitivity to changes in external perturbing factors, opened up the possibility for new applications: temperature and/or pressure sensors, chemical sensors, memory, displays, fast switching devices. Throughout this thesis both theoretical and experimental studies on the possibility of using these materials in the manufacture of temperature sensors and pressure were presented. Using a Ising-like model, we begin with a theoretical investigation of the role of cooperativity in a SCO system, the interactions of surface molecules with their environment, architecture and size effects. We continued the theoretical study using a Atom Phonon coupling model and showed the efficiency of the parabolic method in solving for the system's Hamiltonian. We also performed experimental studies to point out the thermal and piezo-chromic properties of the SCO compounds $[\text{Fe}(\text{hyprtrz})]_2\text{A}_2\cdot\text{H}_2\text{O}$ și $[\text{Fe}(\text{hyetrz})_3]_2\cdot\text{H}_2\text{O}$.

The theoretical studies on the role of a system's cooperativity were carried out using a Ising-like model in combination with a Monte Carlo Entropic Sampling method used to generate all system states. We have shown that behind a multi step transition there are three types of interactions: the short-range interactions, long-range interactions and interactions of surface molecules with their environment. These results are important for the construction of a SCO materials based device. It is also very important to take into account the interactions that can occur between the molecules on the surface with their environment. For example, in the manufacturing process of a SCO based sensor it is important to take into account the interactions that occur between SCO and the support material used to deposit the SCO to, and interactions between SCO and the polymer material used to enclose the SCO material. Interactions between surface molecules and their environment are more important, especially when the system is set up so that the number of molecules at the surface is greater than that of the entire system. We have shown that a 1D system, where the edge only has two molecules, requires a large value of edge interactions in order to play a significant role in SCO system behavior. 2D and 3D systems, where the number of surface molecules is much higher, the SCO system behavior is influenced even for lower values of edge interactions. The influence of edge effect is all the greater as the ratio of molecules on the surface and within the system is higher. These studies were done considering the surface molecules as active molecules.

Important results were obtained from the analysis of the role of system architecture. Considering the same number of molecules we showed that a quadratic system is more cooperative than a rectangular ladder system which in turn is more cooperative than a chain-type system. This is evidenced by the width of the hysteresis loop of each system. It was also revealed that the edge effect shift the transition temperatures to lower values.

Using the Atom Phonon coupling model the results were compared using three different methods of solving the Hamiltonian: mean field approximation, dynamic matrix and the parabolic approximation. Thus we showed that the parabolic approximation method is superior to the approximation of the mean field and that the results obtained by this method are very close to reality. This is because this method uses exact calculation.

The parabolic method leads to the same thermal behavior of the SCO system as that obtained with the dynamic matrix method, especially for small sized system. However, for large systems, the entropy contribution plays an important role and a close correspondence between

results given by these two methods is obtained only for high values of the degeneracy ratio. For example, for $N=8$, this discrepancy disappears for g higher than 1000, that is when the variation of the entropy at the transition temperature is higher than $R\ln(g) = 57.9 \text{ Joule K}^{-1} \text{ mol}^{-1}$. This entropy variation value is common in SCO systems.

Experimental studies were conducted on two SCO compounds: $[\text{Fe}(\text{hyptrz})]\text{A}_2\cdot\text{H}_2\text{O}$ and $[\text{Fe}(\text{hyetrz})_3]\text{I}_2\cdot\text{H}_2\text{O}$ respectively, indicating the thermal and piezo-chromic character of the systems. In the thermal analysis of the external pressure behavior of the first compound, a gas pressure cell was used. This type of cell has the advantage to maintain the hydrostatic nature over the entire range of temperature. Thus it was shown that, by applying an external pressure, the transition temperatures are translated to higher values and the width of the hysteresis loop decreases and eventually disappears after which the transition occurs without hysteresis. The second compound was characterized using several techniques: optical characterization, DSC, Mössbauer spectroscopy and a home-made micromechanical device. We proved the feasibility of pressure detection using a molecular spin crossover based sensor/marker operating at ambient temperature. For the SCO compound $[\text{Fe}(\text{hyetrz})_3]\text{I}_2\cdot\text{H}_2\text{O}$, we obtained a threshold value of the contact pressure of about 30 MPa to irreversibly induce the color change of the molecular material, due to the spin state switching from HS to LS state. Moreover, the possibility of switching back the color using another stimulus (temperature) was demonstrated, making this sensor reusable. As in the previous case, a theoretical investigation in the framework of the Ising-like model has been presented. These results open important perspectives for molecular materials in pressure sensing applications, suggesting the possibility of their insertion in piezo- and thermo-chromic paints that will allow the visual detection of mechanical collisions, a very important issue in the aeronautic and automotive industries.

Taking into account the above mentioned results we proposed a new type of sensor with optical detection that would allow the concomitant detection of both temperature and pressure. This new type of sensor is based on two SCO compounds that exhibit gradual transitions. Considering recent developments in the SCO field this objective could be achievable in the near future.

References

- [1] J. Fraden, Handbook of Modern Sensors, Springer, 2010.
- [2] N. Schroeder, Intechno Consulting Basel (1999).
- [3] Decision Etudes Conseil: European Sensor Industry: Technology, Market and Trends 2007-2011 Paris (2008).
- [4] AMA Fachverband für Sensorik e.V.: Branche/Wirtschaftliche Bedeutung, <http://www.ama-sensorik.de> (2010).
- [5] A.-A.f.S. Technology, Sensor Trends 2014. [http://www.ama-sensorik.de/fileadmin/Publikationen/AMA_Study_Sensor_Trends\[1\].pdf](http://www.ama-sensorik.de/fileadmin/Publikationen/AMA_Study_Sensor_Trends[1].pdf), 2014.
- [6] N. Schroeder, INTECHNO CONSULTING (2012).
- [7] E. Suhir, Springer 2 (2007) 203.
- [8] S. Portal. http://www.sensorsportal.com/DOWNLOADS/Media_Planner_2015.pdf, 2015.
- [9] A.f.S.T.-. AMA, <http://www.ama-sensorik.de/en/association/sector-information/quarterreports-2015/>.
- [10] H.J. Brown-Shaklee, P.A. Sharma, J.F. Ihlefeld, Journal of Materials Science 50 (2015) 5005.
- [11] S. Konstantopoulos, M. Tonejc, A. Maier, R. Schledjewski, J. Reinf. Plast. Compos. 34 (2015) 1015.
- [12] D. Kretschmer, J. Odgers, A.F. Schlader, Journal of Engineering for Power 99 (1977) 1.
- [13] J.D. Goedel, Fast-responding resistance temperature detector (RTD) assembly for various locations such as inlet air in gas turbine engine has thin-walled RTD unit and support structure that minimizes contact with housing to minimize conduction error. UNISON IND LLC (UNIS-Non-standard), p. 27.
- [14] P. Park, D. Ruffieux, K.A.A. Makinwa, Ieee Journal of Solid-State Circuits 50 (2015) 1571.
- [15] <http://www.lakeshore.com/products/cryogenic-temperature-sensors/silicon-diodes/dt-670/pages/Specifications.aspx>.
- [16] <http://www.cryocon.com/S900/S900ds.pdf>.
- [17] Modern sensors handbook, ISTE, London W1T 5DX, UK and Newport Beach, CA 92663 , USA, 2007.
- [18] J. Wajnflasz, R. Pick, J. Phys. Colloques 32 (1971) C1.
- [19] A. Bousseksou, J. Nasser, J. Linares, K. Boukheddaden, F. Varret, Journal De Physique I 2 (1992) 1381.
- [20] J. Linares, H. Spiering, F. Varret, European Physical Journal B 10 (1999) 271.
- [21] Xu, Xiao, X. Yang, L. Zang, Tao, Journal of the American Chemical Society 127 (2005) 2386.
- [22] A. Rotaru, J. Dugay, R.P. Tan, I.A. Gural'skiy, L. Salmon, P. Demont, J. Carrey, G. Molnar, M. Respaud, A. Bousseksou, Advanced Materials 25 (2013) 1745.
- [23] S.V. Aradhya, L. Venkataraman, Nat Nano 8 (2013) 399.
- [24] B. Capozzi, J. Xia, O. Adak, E.J. Dell, Z.-F. Liu, J.C. Taylor, J.B. Neaton, L.M. Campos, L. Venkataraman, Nat Nano 10 (2015) 522.
- [25] J. Linares, E. Codjovi, Y. Garcia, Sensors 12 (2012) 4479.
- [26] C.-M. Jureschi, I. Rusu, E. Codjovi, J. Linares, Y. Garcia, A. Rotaru, Physica B: Condensed Matter 449 (2014) 47.
- [27] C.M. Jureschi, J. Linares, A. Rotaru, M.H. Ritti, M. Parlier, M.M. Dîrtu, M. Wolff, Y. Garcia, Sensors (Basel, Switzerland) 15 (2015) 2388.
- [28] G. Molnar, L. Salmon, W. Nicolazzi, F. Terki, A. Bousseksou, Journal of Materials Chemistry C 2 (2014) 1360.
- [29] O. Kahn, E. Codjovi, Y. Garcia, P.J. vanKoningsbruggen, R. Lapouyade, L. Sommier, in: M.M. Turnbull, T. Sugimoto, L.K. Thompson (Eds.), Molecule-Based Magnetic Materials - Theory, Techniques, and Applications, 1996, p. 298.
- [30] L. Cambi, L. Szegö, Berichte der deutschen chemischen Gesellschaft (A and B Series) 64 (1931) 2591.
- [31] E. König, Chemical Communications 3 (1966) 61.
- [32] E. König, K. Madeja, JACS 88 (1966) 4528.
- [33] E. König, Structure and Bonding 76 (1991) 51.

- [34] R.C. Stoufer, D.H. Busch, W.B. Hadley, *Journal of the American Chemical Society* 83 (1961) 3732.
- [35] J. Zarembowitch, O. Kahn, *Inorganic Chemistry* 23 (1984) 589.
- [36] J. Faus, M. Julve, F. Lloret, J.A. Real, J. Sletten, *Inorganic Chemistry* 33 (1994) 5535.
- [37] K. Heinze, G. Huttner, L. Zsolnai, P. Schober, *Inorganic Chemistry* 36 (1997) 5457.
- [38] W. Eberspach, N. Elmurr, W. Klau, *Angewandte Chemie-International Edition in English* 21 (1982) 915.
- [39] W. Klau, W. Eberspach, P. Gutlich, *Inorganic Chemistry* 26 (1987) 3977.
- [40] A. Hauser, *Spin Crossover in Transition Metal Compounds I*, 2004, p. 49.
- [41] R. Boca, L. Dihan, W. Linert, H. Ehrenberg, H. Fuess, W. Haase, *Chemical Physics Letters* 307 (1999) 359.
- [42] K. Nakatani, J. Sletten, S. Halutdesporte, S. Jeannin, Y. Jeannin, O. Kahn, *Inorganic Chemistry* 30 (1991) 164.
- [43] P.G. Sim, E. Sinn, *Journal of the American Chemical Society* 103 (1981) 241.
- [44] L. Kaustov, M.E. Tal, A.I. Shames, Z. Gross, *Inorg Chem* 36 (1997) 3503.
- [45] H.J. Krokoszinski, C. Santandrea, E. Gmelin, K. Barner, *Physica Status Solidi B-Basic Research* 113 (1982) 185.
- [46] Y. Garcia, O. Kahn, J.P. Ader, A. Buzdin, Y. Meurdesoif, M. Guillot, *Physics Letters A* 271 (2000) 145.
- [47] D.M. Halepoto, D.G.L. Holt, L.F. Larkworthy, G.J. Leigh, D.C. Povey, G.W. Smith, *Journal of the Chemical Society-Chemical Communications* (1989) 1322.
- [48] D.M. Halepoto, D.G.L. Holt, L.F. Larkworthy, D.C. Povey, G.W. Smith, G.J. Leigh, *Polyhedron* 8 (1989) 1821.
- [49] M. Sorai, Y. Yumoto, D.M. Halepoto, L.F. Larkworthy, *Journal of Physics and Chemistry of Solids* 54 (1993) 421.
- [50] C.-M. Jureschi, J. Linares, A. Boulmaali, P. Dahoo, A. Rotaru, Y. Garcia, *Sensors* 16 (2016) 187.
- [51] C. Lefter, V. Davesne, L. Salmon, G. Molnár, P. Demont, A. Rotaru, A. Bousseksou, *Magnetochemistry* 2 (2016) 18.
- [52] C.J. Humphreys, *Nature* 401 (1999) 21.
- [53] P. Gütlich, A.B. Gaspar, Y. Garcia, *Beilstein Journal of Organic Chemistry* 9 (2013) 342.
- [54] T. Mahfoud, G. Molnar, S. Cobo, L. Salmon, C. Thibault, C. Vieu, P. Demont, A. Bousseksou, *Applied Physics Letters* 99 (2011) 053307.
- [55] T. Mahfoud, G. Molnar, S. Bonhommeau, S. Cobo, L. Salmon, P. Demont, H. Tokoro, S.I. Ohkoshi, K. Boukheddaden, A. Bousseksou, *Journal of the American Chemical Society* 131 (2009) 15049.
- [56] C. Lefter, I.y.A. Gural'skiy, H. Peng, G. Molnár, L. Salmon, A. Rotaru, A. Bousseksou, P. Demont, *physica status solidi (RRL) – Rapid Research Letters* 8 (2014) 191.
- [57] V. Legrand, S. Pillet, C. Carbonera, M. Souhassou, J.F. Letard, P. Guionneau, C. Lecomte, *European Journal of Inorganic Chemistry* (2007) 5693.
- [58] S. Pillet, J. Hubsch, C. Lecomte, *European Physical Journal B* 38 (2004) 541.
- [59] N.N. Greenwood, T.C. Gibb, (1971).
- [60] P. Guionneau, F. Le Gac, S. Lakhoufi, A. Kaiba, D. Chasseau, J.F. Letard, P. Negrier, D. Mondieig, J.A.K. Howard, J.M. Leger, *Journal of Physics-Condensed Matter* 19 (2007).
- [61] W. Irlner, G. Ritter, E. König, H.A. Goodwin, S.M. Nelson, *Solid State Communications* 29 (1979) 39.
- [62] T. Granier, B. Gallois, J. Gaultier, J.A. Real, J. Zarembowitch, *Inorganic Chemistry* 32 (1993) 5305.
- [63] S. Decurtins, P. Gutlich, K.M. Hasselbach, A. Hauser, H. Spiering, *Inorganic Chemistry* 24 (1985) 2174.
- [64] A. Hauser, *Chemical Physics Letters* 124 (1986) 543.
- [65] W. Linert, M.C. Grunert, A.B. Koudriavtsev, *Spin Crossover in Transition Metal Compounds Iii*, 2004, p. 105.
- [66] J.P. Martin, J. Zarembowitch, A. Bousseksou, A. Dworkin, J.G. Haasnoot, F. Varret, *Inorganic Chemistry* 33 (1994) 6325.

- [67] N. Moliner, L. Salmon, L. Capes, M.C. Munoz, J.F. Letard, A. Bousseksou, J.P. Tuchagues, J.J. McGarvey, A.C. Dennis, M. Castro, R. Burriel, J.A. Real, *Journal of Physical Chemistry B* 106 (2002) 4276.
- [68] J.A. Rodriguez-Velamazan, M. Castro, E. Palacios, R. Burriel, J.S. Costa, J.F. Letard, *Chemical Physics Letters* 435 (2007) 358.
- [69] W. Morscheidt, J. Jeftic, E. Codjovi, J. Linares, A. Bousseksou, H. Constant-Machado, F. Varret, *Measurement Science & Technology* 9 (1998) 1311.
- [70] E. Codjovi, W. Morscheidt, J. Jeftic, J. Linares, M. Nogues, A. Goujon, O. Roubeau, H. Constant-Machado, A. Desaix, A. Bousseksou, M. Verdaguer, F. Varret, *Molecular Crystals and Liquid Crystals Science and Technology Section a-Molecular Crystals and Liquid Crystals* 334 (1999) 1295.
- [71] A. Rotaru, J. Linares, F. Varret, E. Codjovi, A. Slimani, R. Tanasa, C. Enachescu, A. Stancu, J. Haasnoot, *Physical Review B* 83 (2011) 224107.
- [72] E.D. Loutete-Dangui, E. Codjovi, H. Tokoro, P.R. Dahoo, S. Ohkoshi, K. Boukheddaden, *Physical Review B* 78 (2008).
- [73] K. Boukheddaden, E.D. Loutete-Dangui, E. Codjovi, M. Castro, J.A. Rodriguez-Velamazan, S. Ohkoshi, H. Tokoro, M. Koubaa, Y. Abid, F. Varret, *Journal of Applied Physics* 109 (2011) 013520.
- [74] A. Goujon, F. Varret, K. Boukheddaden, C. Chong, J. Jeftic, Y. Garcia, A.D. Naik, J.C. Ameline, E. Collet, *Inorganica Chimica Acta* 361 (2008) 4055.
- [75] L. Zhang, G.-C. Xu, H.-B. Xu, T. Zhang, Z.-M. Wang, M. Yuan, S. Gao, *Chemical Communications* 46 (2010) 2554.
- [76] J.A. Real, H. Bolvin, A. Bousseksou, A. Dworkin, O. Kahn, F. Varret, J. Zarembowitch, *Journal of the American Chemical Society* 114 (1992) 4650.
- [77] D. Chiruta, J. Linares, P.R. Dahoo, M. Dimian, *Journal of Applied Physics* 112 (2012).
- [78] D. Chiruta, J. Linares, Y. Garcia, P.R. Dahoo, M. Dimian, *European Journal of Inorganic Chemistry* 2013 (2013) 3601.
- [79] D. Boinnard, A. Bousseksou, A. Dworkin, J.M. Savariault, F. Varret, J.P. Tuchagues, *Inorganic Chemistry* 33 (1994) 271.
- [80] Y. Garcia, O. Kahn, L. Rabardel, B. Chansou, L. Salmon, J.P. Tuchagues, *Inorganic Chemistry* 38 (1999) 4663.
- [81] D. Chiruta, J. Linares, Y. Garcia, M. Dimian, P.R. Dahoo, *Physica B: Condensed Matter* 434 (2014) 134.
- [82] D. Chiruta, J. Linares, M. Dimian, Y. Alayli, Y. Garcia, *European Journal of Inorganic Chemistry* 2013 (2013) 5086.
- [83] D. Chiruta, C.-M. Jureschi, J. Linares, P.R. Dahoo, Y. Garcia, A. Rotaru, *The European Physical Journal B* 88 (2015) 1.
- [84] A. Atitoaie, R. Tanasa, C. Enachescu, *Journal of Magnetism and Magnetic Materials* 324 (2012) 1596.
- [85] A. Stancu, C. Enachescu, R. Tanasa, J. Linares, E. Codjovi, F. Varret, *Frontiers in condensed matter physics research* Nova Science Publishers (2006).
- [86] J. Pavlik, R. Boca, *European Journal of Inorganic Chemistry* (2013) 697.
- [87] J. Wajnflasz, *J. Phys. Stat. Solidi* 40 (1970) 537.
- [88] R.A. Bari, J. Sivardiere, *Phys. Rev. B* 5 (1972) 4466.
- [89] M. Sorai, S. Seki, *Journal of the Physical Society of Japan* 33 (1972) 575.
- [90] C.P. Slichter, H.G. Drickamer, *J. Chem. Phys.* 56 (1972) 2142.
- [91] M. Sorai, S. Seki, *J. Phys. Chem. Solids* 35 (1974) 555.
- [92] A. Bousseksou, H. Constantmachado, F. Varret, *Journal De Physique I* 5 (1995) 747.
- [93] J.A. Nasser, *European Physical Journal B* 21 (2001) 3.
- [94] N. Metropolis, A.W. Rosenbluth, M.N. Rosenbluth, A.H. Teller, E. Teller, *The Journal of Chemical Physics* 21 (1953) 1087.
- [95] J. Linares, J. Nasser, K. Boukheddaden, A. Bousseksou, F. Varret, *Journal of Magnetism and Magnetic Materials* 140 (1995) 1507.
- [96] A.M. Apetrei, C. Enachescu, R. Tanasa, L. Stoleriu, A. Stancu, *Physica B: Condensed Matter* 405 (2010) 3673.

- [97] C. Enachescu, M. Nishino, S. Miyashita, L. Stoleriu, A. Stancu, *Physical Review B* **86** (2012) 054114.
- [98] I. Shteto, J. Linares, F. Varret, *Physical Review E* **56** (1997) 5128.
- [99] J. Linares, C. Enachescu, K. Boukheddaden, F. Varret, *Polyhedron* **22** (2003) 2453.
- [100] P. Gütllich, *Zeitschrift für anorganische und allgemeine Chemie* **638** (2012) 15.
- [101] M. Seredyuk, A.B. Gaspar, V. Ksenofontov, S. Reiman, Y. Galyametdinov, W. Haase, E. Rentschler, P. Gutlich, *Chemistry of Materials* **18** (2006) 2513.
- [102] E. Coronado, J.R. Galan-Mascaros, M. Monrabal-Capilla, J. Garcia-Martinez, P. Pardo-Ibanez, *Advanced Materials* **19** (2007) 1359.
- [103] G. Molnar, I.y.A. Gural'skiy, L. Salmon, W. Nicolazzi, C. Quintero, A. Akou, K. Abdulkader, G. Felix, T. Mahfoud, C. Bergaud, C. Bartual-Murgui, C. Thibault, C. Vieu, A. Bousseksou, in: H.R.R.S.G.A.L.C.S.C. Miuez (Ed.), *Photonic Crystal Materials and Devices X*, 2012.
- [104] A.H. Ewald, E. Sinn, *Inorganic Chemistry* **8** (1969) 537.
- [105] E. Codjovi, N. Menendez, J. Jeftic, F. Varret, *Comptes Rendus De L Academie Des Sciences Serie Ii Fascicule C-Chimie* **4** (2001) 181.
- [106] O. Company, <http://olikrom.com/>.
- [107] N.F. Sciortino, K.R. Scherl-Gruenwald, G. Chastanet, G.J. Halder, K.W. Chapman, J.-F. Letard, C.J. Kepert, *Angewandte Chemie-International Edition* **51** (2012) 10154.
- [108] T. Kosone, I. Tomori, C. Kanadani, T. Saito, T. Mochida, T. Kitazawa, *Dalton Transactions* **39** (2010) 1719.
- [109] K. Nishi, H. Kondo, T. Fujinami, N. Matsumoto, S. Iijima, M.A. Halcrow, Y. Sunatsuki, M. Kojima, *European Journal of Inorganic Chemistry* (2013) 927.
- [110] D. Chiruta, J. Linares, M. Dimian, Y. Garcia, *European Journal of Inorganic Chemistry* **2013** (2013) 951.
- [111] K. Boukheddaden, J. Linares, H. Spiering, F. Varret, *European Physical Journal B* **15** (2000) 317.
- [112] M.M. Dîrtu, A. Rotaru, D. Gillard, J. Linares, E. Codjovi, B. Tinant, Y. Garcia, *Inorganic Chemistry* **48** (2009) 7838.
- [113] M.M. Dîrtu, C. Neuhausen, A.D. Naik, A. Rotaru, L. Spinu, Y. Garcia, *Inorganic Chemistry* **49** (2010) 5723.
- [114] C. Lochenie, W. Bauer, A.P. Railliet, S. Schlamp, Y. Garcia, B. Weber, *Inorganic Chemistry* **53** (2014) 11563.
- [115] M.M. Dîrtu, F. Schmit, A.D. Naik, I. Rusu, A. Rotaru, S. Rackwitz, J.A. Wolny, V. Schunemann, L. Spinu, Y. Garcia, *Chemistry* **21** (2015) 5843.
- [116] C.-M. Jureschi, B.-L. Pottier, J. Linares, P. Richard Dahoo, Y. Alayli, A. Rotaru, *Physica B: Condensed Matter* **486** (2016) 160.
- [117] F. Volatron, L. Catala, E. Riviere, A. Gloter, O. Stephan, T. Mallah, *Inorganic Chemistry* **47** (2008) 6584.
- [118] J. Linares, C.-M. Jureschi, A. Boulmaali, K. Boukheddaden, *Physica B: Condensed Matter* **486** (2016) 164.
- [119] A. Muraoka, K. Boukheddaden, J. Linares, F. Varret, *Physical Review B* **84** (2011).
- [120] D. Chiruta, C.-M. Jureschi, J. Linares, Y. Garcia, A. Rotaru, *Journal of Applied Physics* **115** (2014).
- [121] J.A. Nasser, K. Boukheddaden, J. Linares, *European Physical Journal B* **39** (2004) 219.
- [122] J.A. Nasser, *European Physical Journal B* **48** (2005) 19.
- [123] A. Gindulescu, A. Rotaru, J. Linares, M. Dimian, J. Nasser, *Journal of Applied Physics* **107** (2010) 09A959.
- [124] A. Rotaru, J. Linares, E. Codjovi, J. Nasser, A. Stancu, *Journal of Applied Physics* **103** (2008) 07B908.
- [125] J.A. Nasser, S. Topçu, L. Chassagne, M. Wakim, B. Bennali, J. Linares, Y. Alayli, *Eur. Phys. J. B* **83** (2011) 115.
- [126] A. Rotaru, A. Graur, G.-M. Rotaru, J. Linares, Y. Garcia, *Journal of Optoelectronics and Advanced Materials* **14** (2012) 529
- [127] A. Rotaru, A. Carmona, F. Combaud, J. Linares, A. Stancu, J. Nasser, *Polyhedron* **28** (2009) 1684.

- [128] F. Varret, S.A. Salunke, K. Boukheddaden, A. Bousseksou, E. Codjovi, C. Enachescu, J. Linares, *Comptes Rendus Chimie* **6** (2003) 385.
- [129] K. Boukheddaden, J. Linares, E. Codjovi, F. Varret, V. Niel, J.A. Real, *Journal of Applied Physics* **93** (2003) 7103.
- [130] Y. Garcia, P.J. van Koningsbruggen, R. Lapouyade, L. Fournes, L. Rabardel, O. Kahn, V. Ksenofontov, G. Levchenko, P. Gütlich, *Chemistry of Materials* **10** (1998) 2426.
- [131] V. Ksenofontov, H. Spiering, A. Schreiner, G. Levchenko, H.A. Goodwin, P. Gütlich, *Journal of Physics and Chemistry of Solids* **60** (1999) 393.
- [132] Y. Garcia, V. Ksenofontov, G. Levchenko, G. Schmitt, P. Gütlich, *Journal of Physical Chemistry B* **104** (2000) 5045.
- [133] P. Gütlich, A.B. Gaspar, V. Ksenofontov, Y. Garcia, *Journal of Physics-Condensed Matter* **16** (2004) S1087.
- [134] J. Jeftic, N. Menendez, A. Wack, E. Codjovi, J. Linares, A. Goujon, G. Hamel, S. Klotz, G. Syfosse, F. Varret, *Measurement Science & Technology* **10** (1999) 1059.
- [135] A. Rotaru, F. Varret, E. Codjovi, K. Boukheddaden, J. Linares, A. Stancu, P. Guionneau, J.F. Letard, *Journal of Applied Physics* **106** (2009) 053515.
- [136] A. Bhattacharjee, M. Roy, V. Ksenofontov, J.A. Kitchen, S. Brooker, P. Gütlich, *European Journal of Inorganic Chemistry* (2013) 843.
- [137] A. Rotaru, J. Linares, S. Mordelet, A. Stancu, J. Nasser, *Journal of Applied Physics* **106** (2009) 043507.
- [138] Y. Konishi, H. Tokoro, M. Nishino, S. Miyashita, *Physical Review Letters* **100** (2008).
- [139] S. Klokishner, J. Linares, F. Varret, *Chemical Physics* **255** (2000) 317.
- [140] R. Tanasa, A. Stancu, J.F. Letard, E. Codjovi, J. Linares, F. Varret, *Chemical Physics Letters* **443** (2007) 435.
- [141] Y. Garcia, P.J. vanKoningsbruggen, E. Codjovi, R. Lapouyade, O. Kahn, L. Rabardel, *Journal of Materials Chemistry* **7** (1997) 857.
- [142] Y. Garcia, V. Ksenofontov, P. Gütlich, *Hyperfine Interactions* **139** (2002) 543.
- [143] Y. Garcia, P.J. van Koningsbruggen, R. Lapouyade, L. Rabardel, O. Kahn, M. Wiczorek, R. Bronisz, Z. Ciunik, M.F. Rudolf, *Comptes Rendus De L Academie Des Sciences Serie Ii Fascicule C-Chimie* **1** (1998) 523.
- [144] M.M. Dîrtu, F. Schmit, A.D. Naik, A. Rotaru, J. Marchand-Brynaert, Y. Garcia, *International Journal of Molecular Sciences* **12** (2011) 5339.